AD-A156 040 MILLIMETER-WAVE PROPAGATION IN MOIST AIR: MODEL VERSUS PATH DATA (U) NATIONAL TELECOMMUNICATIONS AND INFORMATION ADMINISTRATION BO... H J LIEBE ET AL 1/1

UNCLASSIFIED MAR 85 NTIA-85-171 ARO-21677.1-GS F/G 4/1 NL

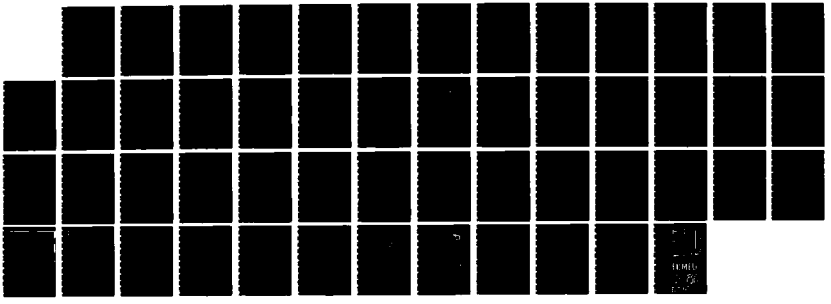

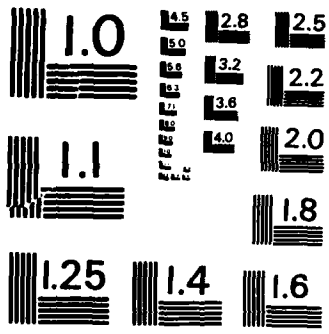

NTIA Report 85-171

Millimeter-Wave Propagation in Moist Air: Model Versus Path Data

H. J. Liebe
K. C. Allen
G. R. Hand
R. H. Espeland
E. J. Violette

NTIA Report 85-171

Millimeter-Wave Propagation in Moist Air: Model Versus Path Data

H. J. Liebe
K. C. Allen
G. R. Hand
R. H. Espeland
E. J. Violette

U.S. DEPARTMENT OF COMMERCE
Malcolm Baldrige, Secretary
David J. Markey, Assistant Secretary
for Communications and Information

March 1985

LIST OF FIGURES

FIGURE — Page

1 Predicted (MPM) specific attenuation α and dispersive delay β up to 1000 GHz for moist sea level air and pure water vapor each for two conditions v = 1 and 30.3(100%RH) g/m³ at T = 30°C 12

2 Predicted specific attenuation α and dispersive delay β for moist air (0-100%RH) at sea level including simulated fog conditions (w = 0.1) with roughly 300 m visibility. Five atmospheric millimeter wave window ranges are marked W1 to W5:

a) T = 5°C and w = 0.1. 13
b) T = 25°C and w = 0. 14

3 Terrain profile of 27.2-km Boulder path with two ray paths for normal (k = 1.34) and subrefractive (k = 0.29) propagation 20

4 Schematic of data acquisition at RX 23

5 Typical daily records of received signal levels $s_{1,2,3}$ and supporting meteorological data for Boulder LOS link (L = 27.2 km) taken at a sampling rate, τ = 1s:

a) relatively quiet atmosphere ("dry" scintillations) . . 26
b) relatively active atmosphere ("moist" scintillations) . 27
c) possible multipath event. 28
d) rain event. 30

6 Predicted specific attenuation α for humid air and temperatures every 10°C ranging from 0° to 40°C at the three frequencies $f_{1,2,3}$ of the Boulder propagation path 32

7 Water vapor attenuation slope $g = [\alpha(v) - \alpha(0)]/v$ as a function of temperature (solid curves are v = const., dashed curves are RH = const.) at different frequencies:

a) Boulder LOS link frequencies. 33
b) H_2O line center frequencies 34
c) atmospheric transmission window frequencies 34

FIGURE		Page
8	Specific attenuation α and refractive dispersion $\Delta N = N'(f_2) - N'(f_2)$ for humid air and temperatures every 10°C ranging from 0° to 40°C at two frequencies $f_{1,2}$ of a Tokyo, Japan, propagation path	38
9	Specific attenuation α for humid air at T = 16° ± 2°C and a frequency of 337 GHz.	40
10	Attenuation rates α at 94 GHz and optical frequencies (visible light) as functions of absolute humidity v and relative humidity RH.	41
11	Water vapor attenuation rates α(v) across the atmospheric window range W4 at two temperatures, 5° and -10°C.	42
12	Water vapor attenuation rates α(v) across the atmospheric window ranges W5 and W6 at two temperatures, 8.5° and 25.5°C	43
13	Water vapor attenuation rate α(v) at 28.8 and 96.1 GHz for a temperature range between -10° and 40°C	47
14	Power spectral density W(ω) and ratios W_2/W_1 for event time series shown in Figure 5:	
	a) see Figure 5a.	48
	b) see Figure 5b.	48
	c) see Figure 5c.	49
	d) Test of FFT.	49

LIST OF TABLES

TABLE		Page
1	Characteristic Time and Horizontal Scales of Atmospheric Processes. . . .	2
2	Spectroscopic Coefficients of Air Due to Oxygen and Water Vapor Lines up to 1000 GHz(Local Line Base)	8
3	Haze and Fog Attenuation α_w and Delay β_w Normalized to w = 1 g/m^3	10
4	Performance Parameters for Boulder LOS Link	22
5	Predicted Specific Attenuation α (dB/km) for a Total Pressure P = 101.3 kPa and Hydrosol Attenuation Factor x_w at Various Relative Humidities RH (%) and Temperatures T(K) for Selected Millimeter-wave Frequencies	36
6	Overview of Experimental Results From Horizontal Line-of-Sight (LOS) Paths, a Mountain Peak Zenith (ZEN) Path, and Laboratory (LAB) Experiments, All Used As Corroborative Data for the Propagation Program MPM	37
7	Summary of an MPM-Analysis of Atmospheric Brightness T_B^x Measured at Frequencies Between 2.5 and 90 GHz from a Mountain Peak	45

LIST OF SYMBOLS

Acronyms

BER	-	bit-error-rate	MST	-	mountain standard time
BW	-	antenna beamwidth	NBS	-	National Bureau of Standards
cw	-	continuous wave	N unit	-	refractivity unit (ppm)
E	-	east	O_2	-	oxygen
FFT	-	fast Fourier transform	ppm	-	parts per million (10^{-6})
fct	-	function	rf	-	radio (millimeter-wave) frequency
H_2O	-	water vapor			
ID	-	curve identification	RSL	-	received signal level
ITS	-	Institute for Telecommunication Sciences	RX	-	receiver site
			TX	-	transmitter site
LAB	-	laboratory experiment	W	-	west
LOS	-	line of sight	W1,2,...		atmospheric transmission windows
MPM	-	millimeter-wave propagation model	ZEN	-	zenith path

Subscripts (frequently used)

e	-	water vapor	T	-	temperature
M	-	mixer	t	-	transmitter
p	-	dry air	v	-	absolute humidity
r	-	receiver	w	-	suspended droplets (hydrosol)
s	-	saturated (100% RH)	x	-	experimental

Symbols

A	(dB)	- path attenuation	$C^2_{n,T,v}$	($m^{-2/3}$)	- structure constants
$A_{T,v}$		- sensitivity coefficients (20)	d	(km)	- path length
			d_o	(km)	- far field distance
$a_{1,2,...6}$		- oxygen line coefficients	e	(kPa)	- water vapor pressure
			F	(dB)	- fade margin
$a_{o,p}$	(ppm/kPa-GHz)	- see (12)	F'(f)	(GHz^{-1})	- Re of line shape fct
B	(ps)	- path delay	F"(f)	(GHz^{-1})	- Im of line shape fct
$b_{1,2,3}$		- water vapor line coefficients	f	(GHz)	- radio frequency
			$f_{1,2,3}$	(GHz)	- test frequencies
b_o	(ppm/kPa-GHz)	- see (13)	G	(dB)	- antenna gain
$b_{e,f}$	(ppm/kPa-GHz)	- see (13)	G(RH)		- growth factor (5)
			g	(dB/km)/(g/m³)	- attenuation slope

Symbols continued

h_o	(km)	- initial height
L_o	(dB)	- free space loss
L	(dB)	- insertion loss
k		- effective Earth radius (Fig. 3)
$\ell_{i,o}$	(m)	- turbulence scale sizes
N	(ppm)	- complex refractivity
N_o	(ppm)	- refractivity
N'(f)	(ppm)	- refractive dispersion
N"(f)	(ppm)	- extinction
n		- integer
$n_{a,b}$		- line number (7)
P_t	(mW)	- rf power
P	(kPa)	- barometric pressure
p	(kPa)	- dry air pressure
Q_r	(dBm)	- receiver noise level
R	(mm/hr)	- rain rate
RH	(%)	- relative humidity
S	(kHz)	- line strength
S_y	(dB)	- system gain
$s_{1,2,3}$	(dB)	- log-amplitude RSL
T	(°C)	- temperature
T_E	(K)	- effect. receiver noise temperature
t	(s)	- time
$u_\perp$	(m/s)	- cross-wind speed
V	(mm)	- path-integrated water vapor
v	(g/m^3)	- absolute humidity
W(ω)	(dB^2/Hz)	- power spectral density
w	(g/m^3)	- hydrosol concentration
w_o	(g/m^3)	- ≡ w(RH = 0%)
x	(km)	- path distance
x_w		- hydrosol factor

α(f)	(dB/km)	- specific attenuation
β(f)	(ps/km)	- specific delay
β_o	(ps/km)	- refractive delay (N_o)
γ	(GHz)	- line width
Δ		- small change
Δf	(MHz)	- bandwidth
δ		- overlap correction
ε', ε"		- dielectric constant of water
$\zeta = (2+\varepsilon')/\varepsilon"$		- see (14)
η		- antenna efficiency factor
θ = 300/T(K)		- relative inverse temperature
λ	(mm)	- wavelength
ν_o	(GHz)	- line center frequency
σ	(ppm^2)	- variance of N
σ_s	(dB^2)	- variance of s
τ	(s)	- sampling rate
τ_w	(ns)	- water relaxation time constant
ω	(Hz)	- fluctuation frequency
ω_o	(Hz)	- corner frequency

MILLIMETER-WAVE PROPAGATION IN MOIST AIR: MODEL VERSUS PATH DATA

H. J. Liebe, K. C. Allen, G. R. Hand, R. H. Espeland, and E. J. Violette*

A practical atmospheric millimeter-wave propagation model (MPM) is updated and tested with experimental data from horizontal, line-of-sight links when there is no precipitation. The MPM computer program predicts attenuation and delay properties of moist air over ranges in frequency from 1 to 1000 GHz and in height from 0 to 30 km. Input variables are radio path distributions of pressure, temperature, relative humidity, and a suspended droplet concentration simulating haze and fog conditions. Terrestrial path data from millimeter-wave propagation experiments, including those from a 27 km link operated at 11.4, 28.8, and 96.1 GHz by the Institute for Telecommunication Sciences (ITS), have been analyzed. Calibrated mean signal levels permitted studies of water vapor losses. In addition, a spectral analysis was performed of clear-air scintillations caused by turbulence. In general, good agreement is obtained with the MPM for test frequencies up to 430 GHz.

Key words: atmospheric attenuation and delay; millimeter wave properties of moist air; propagation program MPM; terrestrial radio path data

1. INTRODUCTION

Atmospheric propagation limitations dominate most considerations in the advancement of millimeter-wave applications (Crane, 1981; Bohlander et al., 1985). Adverse weather causes millimeter-wave signal degradations due to rain, wet snow, suspended particles, and water vapor. A propagation model provides a cost-effective means of predicting the performance of a system for its intended use by considering limiting factors of the atmosphere that in the actual operating environment may be difficult to identify. The Institute for Telecommunication Sciences (ITS) has developed a modular Millimeter-wave Propagation Model labeled MPM (Allen and Liebe, 1983; Liebe, 1983). Based on meteorological variables, the model predicts propagation effects (that is, radio path attenuation, delay, and medium noise) for a radio path through the first 100 km (nominally ground-to-space) of the atmosphere. Frequencies up to 1000 GHz (1 THz) are considered. The model has been used, for example, to provide estimates of millimeter-wave, average-year attenuation distributions for diverse climates across the United States (Allen et al., 1983).

This report addresses the moist air portion of the MPM. Central to the model are more than 450 spectroscopic parameters describing local (<1 THz) absorption lines of the molecules O_2 and H_2O complemented by continuum spectra for dry air,

*The authors are with the Institute for Telecommunication Sciences, National Telecommunications and Information Administration, U. S. Department of Commerce, 325 Broadway, Boulder, Colorado 80303.

water vapor, and hydrosols (i.e., suspended water droplets for haze and fog conditions). Laboratory measurements of absolute attenuation rates at 138 GHz for simulated air with water vapor pressures up to saturation led to an improved water vapor continuum (Liebe, 1984). In addition, other research findings have been reported recently on the spectroscopic data base, which impact predictions and thus warranted an update (Liebe, 1985) of earlier versions (Waters, 1976; Liebe, 1981). The new MPM describes millimeter-wave characteristics of moist air and is presented in Section 2.1 in the form of a comprehensive complex refractivity N.

Terrestrial propagation experiments in the 10 to 100 GHz range have been conducted by ITS over path lengths between 0.1 and 27 km employing cw and broadband (>1 GHz) signals (Violette et al., 1983; Espeland et al., 1984). In order to compare MPM predictions with realistic data, absolute intensity measurements were performed of phase-coherent signals at 11.4, 28.8, and 96.1 GHz over a 27.2 km path located in Boulder, Colorado. Calibrated levels of received signal amplitudes have been processed for time periods free of precipitation to obtain mean values $\bar{s}$(dB) and variances σ_s(dB^2) as indicators for atmospheric losses and fluctuations introduced by water vapor, turbulence, and possible layering effects. Attenuation (dB/km) measurements have been made at 28.8 and 96.1 GHz when the atmosphere was well mixed.

Natural atmospheric fluctuations in density and composition cause variations in the refractivity $N \pm \Delta N$ on various time and space scales outlined in Table 1. Turbulence-induced variability ΔN serves to explain temporal and spatial fluctuations in received signal amplitudes, phases, and angles-of-arrival. Turbulence models addressing amplitude scintillations of millimeter waves are discussed briefly in Section 2.2.

Table 1. Characteristic Time and Horizontal Scales of Atmospheric Processes (Orlanski, 1975)

Process	Approximate Time Scale	Approximate Horizontal Scale
	s	m
Turbulence	10^{-2}-10^{4} (millisec. to hours)	10^{-3}-10^{3} (micro)
Earth rotation	10^{5} (day)	10^{3}-10^{4} (meso)
Weather systems	10^{5}-10^{6} (week)	10^{4}-10^{5} (synoptic)
Seasonal changes	10^{6}-10^{7} (month)	10^{5}-10^{6} (macro)
Weather cycles	10^{7}-10^{9} (year)	10^{6}-10^{7} (global)

Experimental data capable of substantiating these models have been limited to a few cases (e.g., Cole et al., 1978; Filho et al., 1983; Vogel et al., 1984). Scintillation results obtained with the Boulder link for a frequency ratio of 1:6.4, add suitable test data. Section 2.3 touches upon the problem that weak turbulence might sustain large-scale refractive index stratifications. Such conditions might result in deep fade events since stable layering can lead to multiple rays that mutually interfere.

Details of the ITS terrestrial propagation experiment are summarized in Section 3. Observations of received signal strengths obtained with this link, together with simultaneously measured meteorological data, are presented in Section 4. Also included are selected data up to 430 GHz that have been reported in the literature. Section 5 contains the results of various intercomparisons between tractable propagation data from individual events and model results. The report concludes with a discussion of the validity of predictions and their value in forecasting the performance of millimeter wave systems operating through the atmosphere.

2. MILLIMETER-WAVE CHARACTERISTICS OF MOIST AIR

Millimeter waves traversing an atmospheric line-of-sight (LOS) path lose energy in various ways, most of which are frequency-dependent. Radiated energy can be absorbed, scattered out of the path, or diverted by refraction and diffraction effects that cause the signal either to miss the receiving antenna and/or to arrive out of phase with the main ray. All these interactions are dynamic in nature, driven by the variable atmosphere and leading to modulations of the propagating radio wave in amplitude and phase (transit time).

Two basic approaches for predicting transmission characteristics of moist air are taken:

- Physical Model (Section 2.1). Number concentrations of absorbers, refractive layers, and diffraction boundaries as part of the path geometry, all are accounted for based on physical quantities measurable, at least in principle, at any given path location and time.

  The transmission of broadband (>100 MHz) signals adds the additional dimension of frequency response across the signal bandwidth. In digital schemes, dispersive group delay within the atmospheric propagation channel can cause intersymbol interference limiting the maximum data transmission rate. For example, 100 megabit per sec (Mb/s) tolerate about 3 ns deviations from frequency-linear behavior across the bandwidth with no increase in bit error rate (BER).

- Statistical Models (Sections 2.2 and 2.3). Time series of received signal level (RSL) are analyzed in conjunction with meteorological data over time intervals of events specified in Table 1. The RSL is treated as a random variable, disregarding the physical origin of the variability. Typically, a median value is defined over a reference period (e.g., 1 h) superimposed by short-term fluctuations and both processes are evaluated statistically.

2.1 The Propagation Model MPM

The computer program MPM is a physical model developed for applications in telecommunications, radio astronomy, remote sensing, etc., within the 1 to 1000 GHz range (Liebe, 1981; 1985). Radio path behavior through a moist atmosphere is described by cumulative path attenuation

$$A = \int_0^d \alpha(x)dx \qquad \text{dB} \qquad (1a)$$

and by path delay

$$B = \int_0^d \beta(x)dx \qquad \text{ps,} \qquad (1b)$$

where dx is an increment of the path length x in kilometers (km) which is of total length d. Attenuation A quantifies the amount of energy extracted from a plane wave propagating through the atmosphere, delay β is a measure of the excess traveling time with reference to vacuum. Specific power attenuation α and propagation delay β can be expressed in the form

$$\alpha = 0.1820f\, N''(f) \qquad \text{dB/km} \qquad (2a)$$

and

$$\beta = 3.336\, [N_o + N'(f)] \qquad \text{ps/km,} \qquad (2b)$$

where frequency f is in gigahertz (GHz) throughout. The heart of the model is a macroscopic measure of interactions between radiation and the propagation medium, expressed as complex refractivity in N units ($10^{-6} \equiv$ ppm)

$$N = N_o + N'(f) + jN''(f). \qquad (3)$$

The refractivity consists of a frequency-independent term N_o plus various spectra of refractive dispersion N'(f) and absorption N"(f).

Meteorological Parameters

Gaseous oxygen (O_2) and water vapor (H_2O), and suspended water droplets are considered to be the principal absorbers. The physical state of air is described by four measurables P-T-RH-w, which relate to internal model variables p-θ-e(v)-w_o as follows:

$$P = p + e \quad (kPa), \qquad T = (300/\theta) - 273.15 \ (°C),$$

$$RH = (e/e_s)100 \quad (\%), \qquad w = w_o\, G(RH) \quad (g/m^3).$$

Barometric pressure is labeled P, where p is dry air pressure and e is partial water vapor pressure, all in units of kilopascal (1 kPa = 10 mb); temperature T in degrees Celsius (°C) is converted to a relative inverse temperature parameter θ, which for T in absolute Kelvin units equals 300/T(K); and relative humidity

$$RH = (e/e_s)100 = (v/v_s)100 = 41.51\, e\, \theta^{-5}\, 10^{(9.834\,\theta\, -\, 10)} \leq 100\% \qquad (4)$$

is given as absolute humidity ratio described interchangeably by either water vapor partial pressure e or vapor concentration $v = 7.217\, e\, \theta$ (g/m^3). The subscript "s" denotes the saturation limit at RH = 100%. A dry mass concentration of hygroscopic aerosol is w_o in g/m^3 and an approximate expression for the unitless mass growth factor for RH < 96% is given by (Haenel, 1976)

$$G \simeq 100/(100\text{-}RH). \qquad (5)$$

Complex Refractivity N

Radio refractivity of air has been measured accurately at microwave frequencies (e.g., Boudouris, 1963) and reviewed recently (Hill et al., 1982) to be

$$N_o = (2.588\, p + 2.39\, e)\theta + 41.63\, e\, \theta^2. \qquad (6)$$

Absorption and dispersion spectra are obtained from n_a = 48 oxygen lines, n_b = 30 water vapor lines, and various continuum spectra N_p (dry air), N_e (water vapor), and N_w (hydrosol) via

$$d_o = 6.67\ D^2 f\ 10^{-3} \quad \text{km} \quad (27)$$

is exceeded (e.g., f = 96.1 GHz, D = 0.3 m, $d_o \geqq 0.058$ km).

b) Free space loss,

$$L_o = 20 \log (f\ d) + 92.45 \quad \text{dB}, \quad (28)$$

accounts for the decrease in rf power with distance d (km) from an isotropic transmitter antenna (e.g., f = 96.1 GHz, d = 27.2 km, L_o = 160.8 dB).

c) The receiver noise power level equals

$$Q_r = 10 \log (\Delta f\ T_E) - 138.6 \quad \text{dBm}, \quad (29)$$

where T_E is the effective receiver noise temperature (K) which includes mixer rf loss and antenna contributions, and the detection bandwidth Δf is in MHz (e.g., T_e = 1200 K, Δf = 1.0 MHz, Q_r = -107.8 dBm).

To measure the highly variable atmospheric loss A, the following parameter have to be considered for the LOS experiment:

d . . . . . for the propagation path,
P_t, D_t, L_t, f . . . . . for the transmitter,
T_E, D_r, L_r, L_M, Δf . . . . . for the receiver,

in order to ensure, under all conditions, a system performance of F > 0 dB.

3.1 Link Description (27-km Path)

The propagation path was located in Boulder, CO, and had a length d = 27.2 km. The first 7-km segment starting at the receiver terminal is across the city of Boulder and the remainder is over open fields and farms. This path runs generally parallel to the foothills on the west, approximately 5 to 7 km from the first mountain ridge. Receiver and transmitter terminal locations at h(RX) = 1.654 and h(TX) = 1.646 km elevation, respectively, and a cross section of the propagation path are shown in Figure 3. Antenna beamwidths BW at the operating frequencies are indicated as well as ray paths for a standard (k = 1.34, effective Earth radius) and a subrefractive (k = 0.29) constant refractivity gradient (e.g., Stephansen, 1981), where the latter condition would cause the ray to just touch the ground in the middle of the path.

(RSL) $s_{1,2,3}$ (dB) qualified the field experiment for testing predictions made with propagation models discussed in Section 2. Examples of daily RSL recordings, free of precipitation, are presented and a power-spectral analysis of relatively quiet and relatively active fade periods is performed.

Together with the three cw channels, a wide-band channel was operated using a 30.3 GHz carrier with a 500 Mb/s biphase-shift-key modulator and a 1 ns resolution impulse probe (Violette et al., 1983). Bit-error-rates (BER) were measured down to about 2×10^{-8} for a 1 second gate-time and a pseudo-random code. In clear weather, the error rates stayed usually below the detection threshold and are of no concern in this report.

Performance of an LOS system is evaluated by the signal-to-noise ratio (fade margin)

$$F = S_y - L_o - Q_r - A \qquad \text{dB} \qquad (24)$$

realized at the receiver. The quantities in (24) represent a system gain S_y, the free space loss L_o, receiver noise power N_r, and atmospheric propagation loss A (1a); all but A are examined in more detail in the following.

a) A system gain factor

$$S_y = 10 \log P_t + G_t + G_r - L_t - L_r - L_M \qquad \text{dBm} \qquad (25)$$

is the sum of various hardware contributions, where P_t is the average transmitter power in milliwatts, G_t is the directional gain of the transmitter antenna toward the receiver; G_r is the directional gain of the receiver antenna toward the transmitter; L_t and L_r are rf losses of transmitter and receiver antenna feeds, respectively; and L_M is a conversion efficiency (loss) of the receiver front-end. Parabolic dish antennas, the type typically used in millimeter-wave systems, display a maximum directional gain

$$G_A = 20 \log (fD) + 10 \log \eta + 20.4 \text{ dB} \qquad (26)$$

where D is the antenna diameter in meters, and η_A is the efficiency factor for a particular design (e.g., f = 96.1 GHz, D = 0.30 m, η = 0.6, G = 47 dB). Geometric dish imperfections, illumination blockage, and aperture-to-medium coupling loss decrease the efficiency η. Full antenna gain G is realized when a minimum distance (far-field range)

atmospheric conditions (weak turbulence) plus rapid, height-dependent reductions in water vapor concentration (e.g., fog over moist river valleys during calm, cool nights, and early mornings of hot, summer weather). Under such conditions a radio ray can be trapped and channeled in a duct, where the normal spherical spreading loss L_o (see Section 3) is no longer valid and possible dispersive propagation velocities exist. The result is a strong short-term RSL variability due to more than one component of the radio field arriving at the receiver by way of separate, slightly differing paths. Occasionally, when only two rays interfere with each other, both being of similar magnitude, the RSL can behave very erratically, with unpredictable deep fades in the range of 20 to 40 dB and serious amplitude distortions across the propagation channel bandwidth. Multipath effects present problems for the transmission of digital data. Delay spread causes the received symbols to overlap. The resulting intersymbol interference leads to decoding errors. For example, a delay difference of 3 ns can raise the BER at data transmission rates greater than 30 Mb/s . A channel transmission model capable of simulating three-ray multipath fades was given by Rummler (1979).

Multipath fading can also be expected when reflections occur from terrain features such as hills, buildings, trees, etc. The fade depth depends on the path clearance, surface curvature, surface roughness, etc. A strong specular component will produce regular ($\lambda/2$) interference patterns when the receiving antenna is moved in space. Another phenomenon is obstacle fading due to weather-dependent refractivity changes. The effective earth radius (typically 4/3) changes so that vertical clearances become marginal from large-sized obstacles (hills, the ground, buildings, tree tops, etc.) close to the LOS path. These fades are not particularly frequency-sensitive.

It is possible to reduce the effect of multipath fading in a number of ways; the most common are narrower beamwidth, antenna tilts, space and frequency diversity and good path clearances.

3. BOULDER LOS EXPERIMENT

A terrestrial line-of-sight (LOS) link designed to investigate atmospheric millimeter-wave propagation (Violette et al., 1983; Espeland et al., 1984) was operated over a 27.2-km path near Boulder, CO, between August 9, 1983, and June 14, 1984. The link was outfitted at the receiver site with meteorological instrumentation. Three phase-coherent channels at f_1 = 11.4 GHz, f_2 = 28.8 GHz, f_3 = 96.1 GHz provided amplitude data suitable to analyze atmospheric loss and fade mechanisms and evaluate frequency-dependent responses. Absolute calibration of the received signal levels

$$c_v^2/c_T^2 \cong 10^4 \langle v\rangle^2/\langle T\rangle^2, \qquad (21)$$

and humidity variance dominates the refractivity structure. The resulting c_n^2 values are large ("moist" fluctuations). The structure constant is highest in layers nearest the ground where millimeter-wave values for c_n^2 can range between 10^{-12} and 10^{-17} $m^{-2/3}$.

The refractivity N given by (3) is complex. Terms should be added to (17) to account for contributions from the variance of absorption and the covariance of refraction and absorption (Ott and Thompson, 1978; Hill and Clifford, 1981). Usually, humidity variations dominate the structure constant c_n^2 via refraction , and the contribution of absorption to fluctuations will be difficult to observe in the millimeter-wavelength range, unless specific values of about 5 dB/km are exceeded (Filho et al., 1983).

When a wind with average speed $u_\perp$ (m/s) transverse to the propagation path carries the spatial structure of refractivity fluctuations through the propagation path, a modulation spectrum of scintillation frequencies ω (Hz) is imposed upon the propagating wave. Between inner and outer scales of turbulence a spatial spectrum exists which has a theoretical (Kolmogorov) foundation. Turbulence structures larger than the size of the 1st Fresnel zone produce signal scintillations with constant spectral power density W_o(dB^2/Hz). These occur in the lower frequency portion of the spectrum. The power density falls off rapidly ($\omega^{-8/3}$) with increasing frequencies ω. The spectral asymptotes W_o and $\omega^{-8/3}$ cross at the "corner" frequency

$$\omega_o \cong u_\perp/\sqrt{\lambda d} = 0.058\ u_\perp\sqrt{f/d} \quad \text{Hz}. \qquad (22)$$

The spectral power density for the range $\omega >> \omega_o$ is proportional to (Cole et al., 1978)

$$W(\omega) \propto f^2\ c_n^2\ d\ \ell_i^{5/3} \qquad dB^2/\text{Hz}. \qquad (23)$$

Structure sizes larger than ℓ_o are ill-defined in form. Turbulent phenomena merge with large-scale variations in the atmosphere. A power spectrum $W(\omega)$ should reveal the processes discussed and allow the deduction of a relative refractive structure constant $c_n^2 \propto W_o(\omega)$ and wind speed $u_\perp$ via (17) and (22).

2.3 Multipath Fading

In some regions of the world, frequency-selective fading phenomena from atmospheric refractive layers are fairly common. They are associated with stable

The propagation experiment described in Section 3 yields time series s(t) of log-amplitude behavior at three frequencies f. Under atmospheric conditions where (16) is valid, the variance of log-amplitude scintillations is expected to be proportional to (Vogel et al., 1984)

$$\sigma_s \propto f^{7/6} d^{11/6} c_n^2 \qquad dB^2 \tag{17}$$

Also, it is assumed that the transmitting and receiving antenna sizes are small relative to an approximate 1st Fresnel zone clearance $\sqrt{\lambda d}$, and in turn, the Fresnel zone is small compared with the outer turbulence scale ℓ_o. The radio wavelength λ follows from

$$\lambda = 299.8/f \qquad mm. \tag{18}$$

Since both air density and absolute humidity v affect the refractivity N, the structure parameter c_n^2 can be expressed in terms of analogous parameters for temperature, humidity, and barometric pressure. Neglecting pressure variations, c_n^2 is given by

$$c_n^2 = A_T^2 \frac{c_T^2}{\langle T \rangle^2} + A_v^2 \frac{c_v^2}{\langle v \rangle^2} + 2A_T A_v \frac{c_{Tv}}{\langle T \rangle \langle v \rangle} \qquad m^{-2/3}, \tag{19}$$

where the sensitivity coefficients $A_{T,v}$ are calculated from the refractivity N_o (Hill and Clifford, 1981). The last term in (19) can be approximated by

$$\frac{c_{Tv}}{\langle T \rangle \langle v \rangle} \cong \pm \left[\frac{c_v^2}{\langle v \rangle^2} + \frac{c_T^2}{\langle T \rangle^2} \right]^{1/2} . \tag{20}$$

The positive sign usually applies during the day and the negative sign during the night, due to a change in the direction of the temperature gradient near the ground. Under some dry conditions (Liebe and Hopponen, 1977), (20) can substantially cancel the contribution of the other two terms and result in a situation for which the value of c_n^2 is small ("dry" scintillations). Frequently, the ground evaporates water vapor. In these instances, humidity fluctuations will surpass, in relative terms, temperature fluctuations by far, say

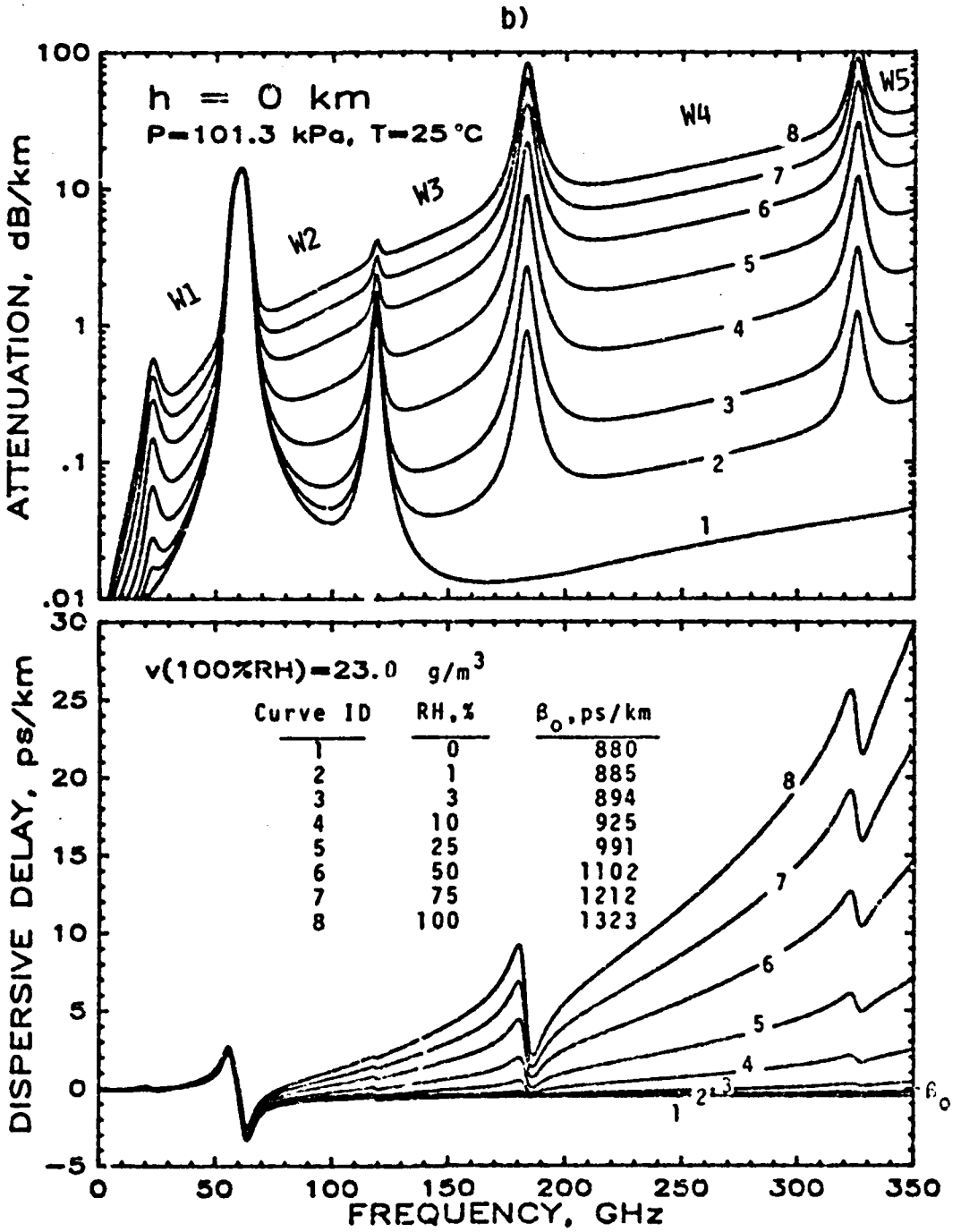

Figure 2. continued. b) T = 25°C and w = 0

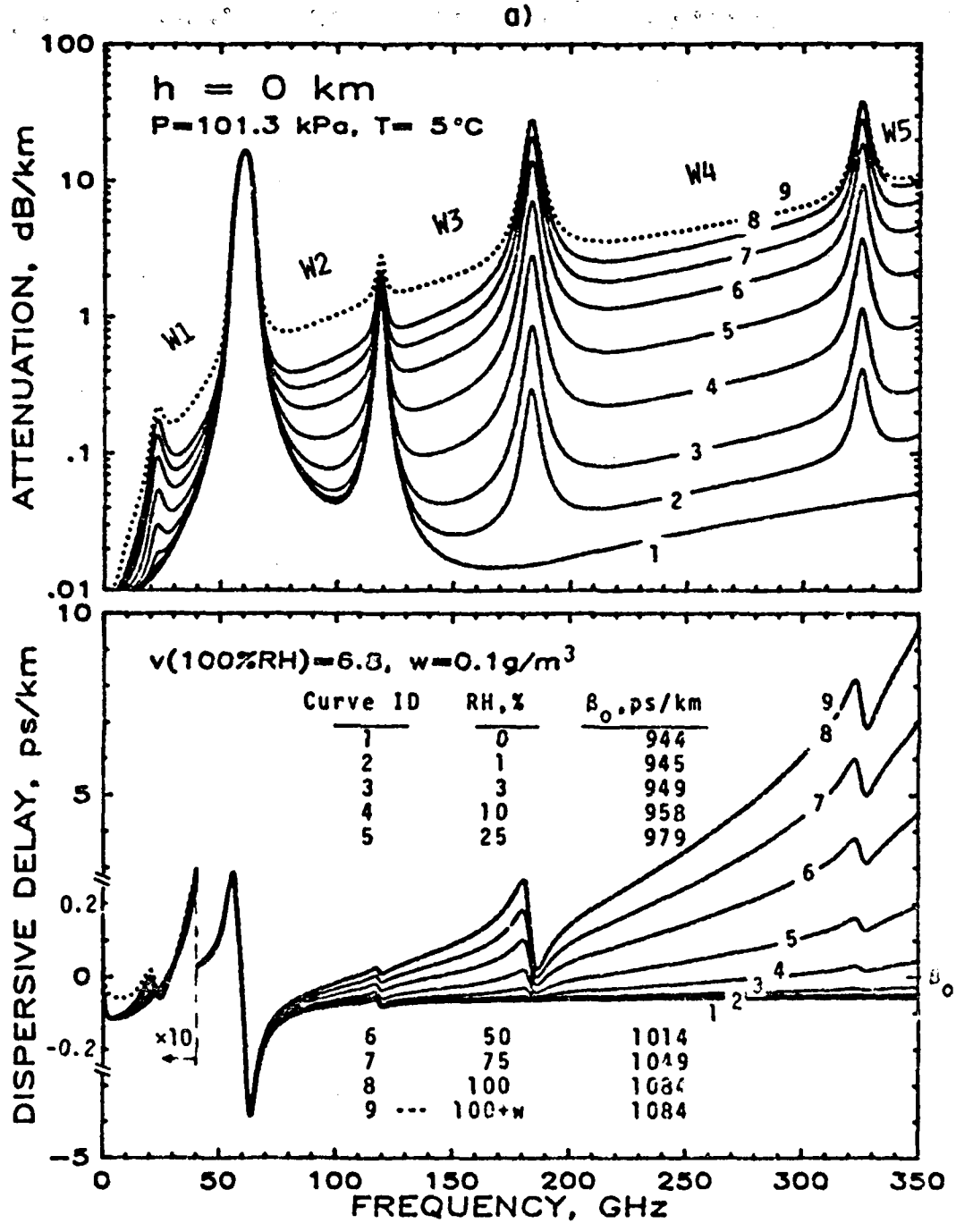

Figure 2. Predicted specific attenuation α and dispersive delay β for moist air (0-100%RH) at sea level including simulated fog conditions (w = 0.1) with roughly 300 m visibility. Five atmospheric millimeter wave window ranges are marked W1 to W5 ($\beta_0 = 3.336\ N_0$, refractive delay): a) T=5°C and W=0.1

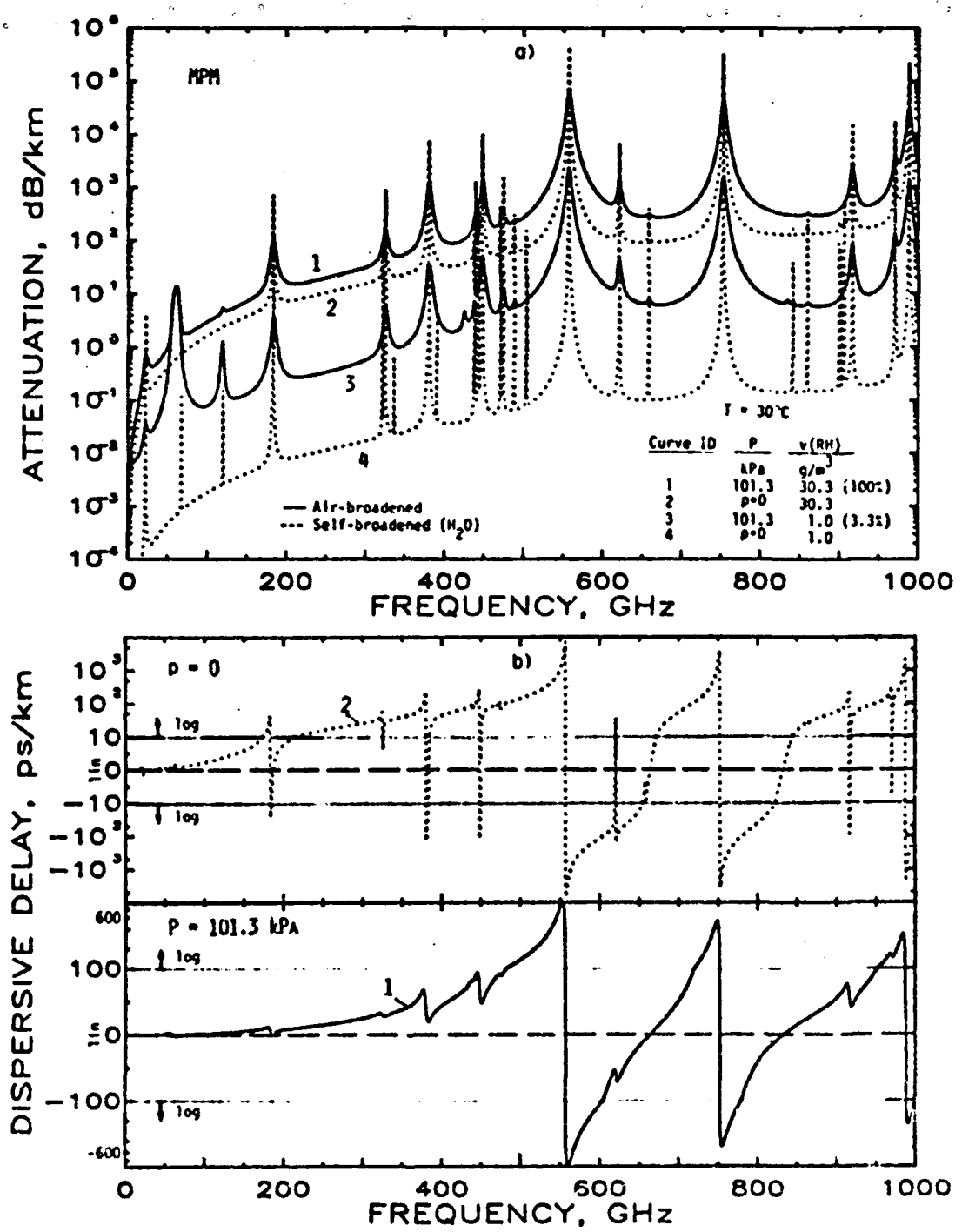

Figure 1. Predicted (MPM) specific attenuation α (a) and dispersive delay β (b) up to 1000 GHz for moist sea level air (#1 and 3) and pure water vapor (#2 and 4) each for two conditions v = 1 and 30.3 (100%RH) g/m^3 at T = 30°C (Note the linear-log scales used to display delay β)

In summary, (1) to (15) constitute the physical MPM, which is capable of predicting millimeter wave properties of moist air for given sets of P-T-v(RH)-w distributions along a radio path. A full range of MPM coverage (i.e., $\alpha(f) = 10^{-4}$ to 10^{6} dB/km, $\beta(f) = \pm 10^{4}$ ps/km, f = 1 to 1000 GHz) is exhibited in Figure 1 for two cases [v = 1 and 30.3(100%RH) g/m^3], each for pure water vapor (H_2O self-broadening) and moist sea level air. Examples in Figure 2 show the humidity dependence of specific attenuation α and dispersive delay β for sea level conditions (P = 101.3 kPa, RH = 0 to 100%, w = 0.1 g/m^3, T = 5 and 25°C) and frequencies up to f = 350 GHz. Five atmospheric transmission windows are indicated by W1 to W5.

Starting from a given choice of mean atmospheric conditions, it is the fluctuations in P-T-v-w that modulate the average moist air refractivity $\bar{N} \pm \Delta N(t,x)$ in space and time which, in turn, influences the propagating radio wave. To evaluate the resulting propagation effects, it is necessary to investigate the stochastic functions that govern atmospheric fluctuations. The practical effects of refractivity $\bar{N}$ and its variance σ are to produce phenomena that may be grouped into those resulting from small-scale turbulence structures (see Section 2.2) and those from large-scale structures in the atmosphere, such as diurnal and weather changes, overall temperature and water vapor distributions including inversions, etc. The latter manifest themselves in effects such as ray bending, ducting, propagation delay dispersion, and multipath interference (see Section 2.3).

2.2 Atmospheric Turbulence

The theory of wave propagation in a turbulent medium, as described by Tatarski (1961), was extended to millimeter waves by Clifford and Strohbehn (1970), Ishimaru (1972), Ott and Thompson (1978), and Hill and Clifford (1981), among others. Submillimeter wave turbulence effects have been treated recently in a review by Bohlander et al. (1985). Under ideal assumptions that turbulent eddies are distributed within a propagation path in an isotropic and homogeneous manner, the structure function at separation Δx can be written as

$$\sigma = \langle \Delta N^2 \rangle = c_n^2 \, \Delta x^{2/3} \, 10^{12}, \qquad (16)$$

where < > denotes ensemble averages, usually replaced by time averages. The separation Δx of two measurement points has to be between an inner scale ℓ_i ($\lesssim$ 0.01 m) and an outer scale ℓ_o($\gtrsim$ 5 m), and c_n^2 in units of m$^{-2/3}$ is called the refractive structure constant. This parameter is the key in relating turbulence to propagation effects such as amplitude scintillations, phase front distortions, and variations in angle-of-arrival.

can be used instead of (14a), based on data reported by Simpson et al. (1979).

The dielectric data $\varepsilon', \varepsilon''$ of bulk water are calculated with the Debye model, which is valid for $f \leq 300$ GHz as reported by Chang and Wilheit (1979):

$$\varepsilon'' = (185 - 113/\theta) f\tau_w / [1 + (f\tau_w)^2] \qquad (15a)$$

and

$$\varepsilon' = 4.9 + (185 - 113/\theta)/[1 + (f\tau_w)^2], \qquad (15b)$$

where $\tau_w = 4.17 \times 10^{-5}\ \theta \exp(7.13\ \theta)$ ns. Table 3 lists numerical examples of $\alpha_w = 0.182 f N''_w$ (dB/km) for two temperatures (0°C and 25°C) at selected frequencies. A strong temperature dependence can be noticed.

Haze conditions are related to vapor-to-droplet conversion processes reversible (swelling/shrinking) with relative humidity for values below RH = 100 percent. The simple growth function (5) provides an approximation of the RH-reversible conversion up to RH ≅ 96 percent. Typical dry air mass loadings of hygroscopic aerosol in ground level air are below $w_o \cong 10^{-4}$ g/m^3. A practical growth function covering the range above RH = 96 percent, including the irreversible condition of supersaturation, RH>100 percent, is lacking. Such a function is needed to explain the growth of suspended droplet concentrations to values $w = 10^{-3}$ to 1 g/m^3 as observed under various fog conditions. At present, reported values for w are used in (14) and the contributions are added to respective calculations (7) for saturated (100%RH) air.

Table 3.

Haze and Fog Attenuation α_w and Delay β_w Normalized to w = 1 g/m^3

TEMPERATURE	FREQUENCY f (GHz)									
T	1	10	30	100	200	300	400	600	800	1000
°C	α_w (dB/km)									
0	.0010	.097	.82	5.4	9.3	10.8	13	18	23	29
25	.0005	.051	.45	4.2	10.8	15.3	21	31	40	48
	β_w (ps/km)									
0	.69	.32	.09	.04	.04	.04	0	0	0	0
25	.62	.49	.20	.06	.04	.04	0	0	0	0
	(14 a,b)						(14c)			

make a small contribution at ground level pressures due to the nonresonant O_2 spectrum below 10 GHz and a pressure-induced N_2 spectrum, effective above 100 GHz (Stankevich, 1974). A width parameter for the Debye spectrum of O_2 is formulated in accordance with (10) to be $\gamma_o = 5.6 \times 10^{-3}(p + 1.1e)\theta^{0.8}$ (GHz) (Rosenkranz, 1982). The continuum coefficients are $a_o = 3.07 \times 10^{-4}$, (Rosenkranz, 1975), and $a_p = 1.17 \times 10^{-10}$ (Dagg et al., 1982).

The water vapor continuum is an empirical contribution derived from fitting experimental data in the case of N_e'' and theoretical data in the case of N_e', which led to

$$N_e''(f) = [b_f p + b_e e\theta^3]f\, e\, \theta^{2.5} \tag{13a}$$

and

$$N_e'(f) = b_o e\, \theta^{2.4} f^{2.05}, \tag{13b}$$

where $b_o = 6.47 \times 10^{-6}$ (R. Hill, personal communications, 1984), $b_f = 1.40 \times 10^{-6}$ and $b_e = 5.41 \times 10^{-5}$ (Liebe, 1984).

2.1.3 Hydrosol Continuum (Haze and Fog)

Suspended water droplets (hydrosols) in haze and fog (or clouds) are millimeter wave absorbers. Their size range of radii is below 50 μm, which allows the Rayleigh approximation to Mie scattering theory to be used for calculating refractivity contributions N_w to (7) in the form (Liebe, 1981; Falcone et al., 1982)

$$N_w''(f) = 4.50w/\varepsilon''(1 + \zeta^2) \tag{14a}$$

and

$$N_w'(f) = 2.4 \times 10^{-3} w\, \varepsilon', \tag{14b}$$

where $\zeta = (2 + \varepsilon')/\varepsilon''$; and $\varepsilon', \varepsilon''$ are real and imaginary parts of the dielectric constant for water. For frequencies above 300 GHz, the following approximation

$$N_w''(f) = 0.55w\, f^{-0.1}\theta^{-6} \tag{14c}$$

Table 2. Spectroscopic Coefficients of Air Due to Oxygen and Water Vapor Lines Up to 1000 GHz (Local Line Base)

ν_o	a_1	a_2	a_3	a_4	a_5	a_6
GHz	$(Hz/kPa)10^{-3}$		MHz/kPa		10^{-3}/kPa	
49.452379	0.12	11.833	9.40	0	5.60	1.7
49.962257	0.38	10.720	9.50	0	5.60	1.7
50.474238	0.94	9.690	8.60	0	5.60	1.7
50.987749	2.46	8.690	8.70	0	5.50	1.7
51.503350	6.08	7.740	8.90	0	5.60	1.8
52.021409	14.14	6.840	9.20	0	5.50	1.8
52.542393	31.02	6.000	9.40	0	5.70	1.8
53.066446	64.10	5.220	9.70	0	5.30	1.9
53.595748	124.70	4.480	10.00	0	5.60	1.8
54.129998	228.00	3.810	10.20	0	4.80	2.0
54.671197	391.80	3.190	10.50	0	4.80	1.9
55.221365	631.60	2.620	10.79	0	4.17	2.1
55.783600	953.50	2.115	11.10	0	3.75	2.1
56.264774	548.90	0.010	16.46	0	7.78	0.9
56.363399	1344.00	1.655	11.44	0	2.97	2.3
56.968180	1741.00	1.255	11.81	0	2.12	2.5
57.612451	2141.00	0.910	12.21	0	0.94	3.7
58.323874	2386.00	0.621	12.66	0	-0.55	-3.1
58.446589	1847.00	0.079	16.49	0	5.97	0.8
59.164204	2654.00	0.386	13.19	0	-2.44	0.1
59.590983	2812.00	0.207	13.60	0	3.44	0.5
60.306057	2124.00	0.207	13.82	0	-4.13	0.7
60.434776	2461.00	0.386	12.97	0	1.32	-1.0
61.150560	2504.00	0.621	12.48	0	-0.36	5.8
61.800154	2099.00	0.910	12.07	0	-1.59	2.9
62.411212	1933.00	1.255	11.71	0	-2.66	2.3
62.486253	1517.00	0.078	14.68	0	-4.77	0.9
62.997974	1503.00	1.660	11.39	0	-3.34	2.2
63.568518	1087.00	2.110	11.08	0	-4.17	2.0
64.127764	733.50	2.620	10.78	0	-4.48	2.0
64.678903	463.50	3.190	10.50	0	-5.10	1.8
65.224547	274.80	3.810	10.20	0	-5.10	1.9
65.764779	153.00	4.480	10.00	0	-5.70	1.9
66.302096	80.09	5.220	9.70	0	-5.50	1.8
66.836829	39.46	6.000	9.40	0	-5.90	1.7
67.369595	18.32	6.840	9.20	0	-5.60	1.8
67.900562	8.01	7.740	8.90	0	-5.80	1.7
68.431001	3.30	8.690	9.70	0	-5.70	1.7
68.96[illegible]306	1.28	9.690	9.60	0	-5.60	1.7
69.489281	0.47	10.720	9.50	0	-5.60	1.7
70.017342	0.16	11.830	8.60	0	-5.60	1.7
118.750343	945.00	0.000	16.92	0	-0.44	0.9
368.498350	67.90	0.270	19.20	0.6	0	1
424.763020	638.00	0.011	19.16	0.6	0	1
487.249273	235.00	0.011	19.20	0.6	0	1
715.393150	99.60	0.269	18.10	0.6	0	1
773.839490	671.00	0.079	16.10	0.6	0	1
834.145331	180.00	0.079	18.10	0.6	0	1

ν_o	b_1	b_2	b_3
GHz	kHz/kPa		MHz/kPa
22.235080	0.1090	2.143	27.84
67.813960	0.0011	8.730	27.60
119.995940	0.0007	8.347	27.00
183.310117	2.3000	0.653	28.35
321.225644	0.0464	6.156	21.40
325.152919	1.5400	1.515	27.00
336.187000	0.0010	9.802	26.50
380.197372	11.9000	1.018	27.60
390.134508	0.0044	7.318	19.00
437.346667	0.0637	5.015	13.70
439.150812	0.9210	3.561	16.40
443.018295	0.1940	5.015	14.40
448.001075	10.6000	1.370	23.80
470.888947	0.3300	3.561	18.20
474.689127	1.2800	2.342	19.80
488.491133	0.2530	2.814	24.90
503.568532	0.0374	6.693	11.50
504.482692	0.0125	6.693	11.90
556.936002	510.0000	0.114	30.00
620.700807	5.0900	2.150	22.30
658.006500	0.2740	7.767	30.00
752.033227	250.0000	0.336	28.60
841.073593	0.0130	8.113	14.10
859.865000	0.1330	7.989	28.60
899.407000	0.0550	7.845	28.60
902.555000	0.0380	8.360	26.40
906.205524	0.1830	5.039	23.40
916.171582	8.5600	1.369	25.30
970.315022	9.1600	1.842	24.90
987.926764	138.0000	0.178	28.60

The line parameters are calculated according to the scheme below:

Symbol	O_2 lines in air	H_2O lines in air	
S , kHz	$a_1 p\theta^3 10^{-6} \exp[a_2(1-\theta)]$	$b_1 e\theta^{3.5} \exp[b_2(1-\theta)]$	(9)
γ , GHz	$a_3(p\theta^{(0.8-a_4)} + 1.1e\theta)10^{-3}$	$b_3(p\theta^{0.8} + 4.80e\theta)10^{-3}$	(10)
δ	$a_5 p\theta^{a_6} 10^{-3}$	0	(11)

Line center frequencies ν_o and the spectroscopic coefficients a_1 to a_6, b_1 to b_3 for strength S, width γ, and overlap correction δ are listed in Table 2.

Standard line shapes F"(f), including the Van Vleck-Weisskopf function (8), predict in frequency regions of local line dominance about the same results for N"(f) as long as F"(f) values are larger than 0.1 percent the peak value at $f = \nu_o$. Wing contributions that are less than 0.1 percent depend upon the chosen line shape function. Far-wing contributions (< 0.001 percent) differ by as much as 1:80 (Liebe, 1984). No line shape has been confirmed that predicts absorption intensities over ranges (10^{-3} to $<10^{-6}$) of $F"(\nu_o)$, as required for the water vapor spectrum. Expected far-wing contributions from strong (> 10^6 dB/km) infrared lines are accounted for summarily by empirical correction.

2.1.2 Continuum Spectrum for Air

Continuum spectra in (7) identify dry air and water vapor terms $N_p + N_e$ and must be added to the selected group of local O_2 and H_2O resonance lines (Table 2) described by (8) in order to correctly predict atmospheric millimeter wave attenuation in window ranges between lines. Continuum absorption increases monotonically with frequency.

The dry air continuum

$$N"_p(f) = \left\{(2a_0\gamma_0[1 + (f/\gamma_0)^2][1 + (f/60)^2]\right\}^{-1} + p\, a_p \Big\} f\, p\, \theta^2 \qquad (12a)$$

and

$$N'_p(f) = a_0\{[1 + (f/\gamma_0)^2]^{-1} - 1\} p\, \theta^2 \qquad (12b)$$

$$N''(f) = \sum_{i=1}^{n_a} (SF'')_i + N''_p + \sum_{i}^{n_p} (SF'')_i + N''_e + N''_w \qquad (7a)$$

and

$$N'(f) = \sum_{i=1}^{n_a} (SF')_i + N'_p + \sum_{i}^{n_p} (SF')_i + N'_e + N'_w \qquad (7b)$$

dry air + water vapor + susp. droplets.

In the line-by-line calculations, S is a line strength in kHz and F' and F'' are real and imaginary parts of a shape function in GHz^{-1}. Pressure broadening of the dominant lines leads to two different types of frequency responses, namely sharp resonance lines and continuum spectra. Both are treated in the following for atmospheric conditions up to heights of h = 30 km. Self- and foreign-gas-broadening influences have to be taken into account. Trace gas spectra are neglected since their abundance is too small to markedly affect tropospheric propagation.

2.1.1 Local Line Absorption and Dispersion

The Van Vleck-Weisskopf function was modified by Rosenkranz (1975) to describe, to first order, line overlap effects. This leads to local absorption and dispersion line profiles

$$F'' = \left(\frac{\gamma - (\nu_o - f)\delta}{(\nu_o - f)^2 + \gamma^2} + \frac{\gamma - (\nu_o + f)\delta}{(\nu_o + f)^2 + \gamma^2} \right) \left(\frac{f}{\nu_o} \right) \quad GHz^{-1} \qquad (8a)$$

and

$$F' = \left(\frac{\nu_o - f + \gamma(\gamma + f\delta)/\nu_o}{(\nu_o - f)^2 + \gamma^2} + \frac{\nu_o + f + \gamma(\gamma - f\delta)/\nu_o}{(\nu_o + f)^2 + \gamma^2} - \frac{2}{\nu_o} \right) GHz^{-1}. \qquad (8b)$$

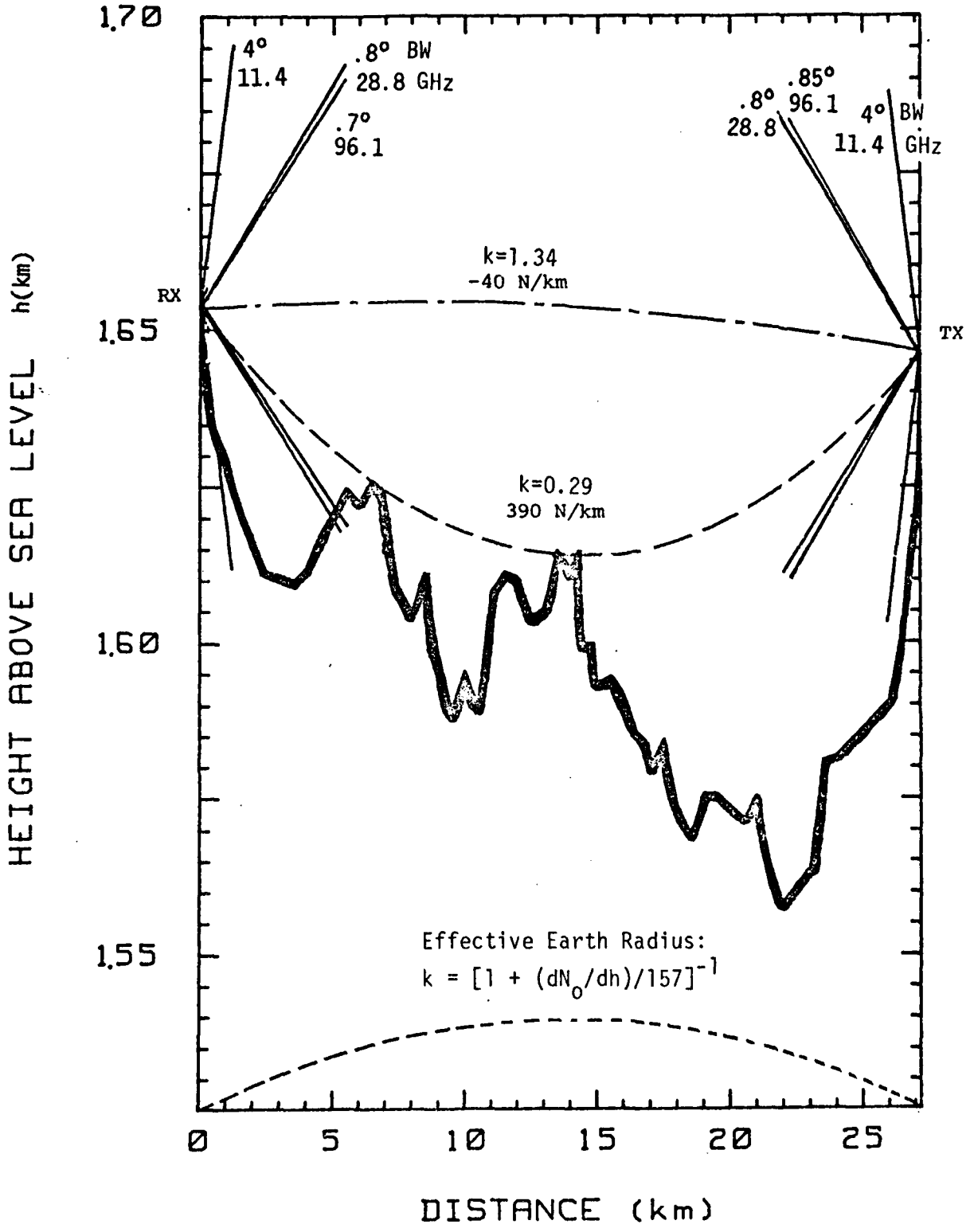

Figure 3. Terrain profile of 27.2-km Boulder path with two ray paths for normal (k=1.34) and subrefractive (k=0.29) propagation (Espeland et al., 1984; Stephansen, 1981):

RX = receiver site in center of Boulder
TX = transmitter site north of town

Full details of the transmitter and receiver configurations have been given by Espeland et al. (1984). All salient parameters that are needed to make a performance assessment (24)-(29) for each of the three channels are summarized in Table 4. The cw carriers are phase-locked to a 100 MHz crystal oscillator. Transmitters and receivers both are located inside protective, temperature-controlled (39° ± 1 °C) structures. Link gain stability is maintained at ± 0.5 dB over an ambient temperature range from -25°C to + 35°C.

Meteorological data are recorded only at the receiving terminal which is, admittedly, insufficient to capture atmospheric activity over the entire path. The meteorological instrumentation measures in situ (RX) microwave (9.375 GHz) refractivity N_o (6), ambient air temperature T, and barometric pressure P. From these parameters, water vapor pressure e and relative humidity RH are calculated using equation (6), (30). The following uncertainties for the sensors have been estimated:

$$\Delta N_o = \pm 0.5 \text{ ppm}, \quad \Delta T = \pm 0.5°C, \quad \text{and } \Delta P = \pm 0.1 \quad (\Delta e = \pm 0.03) \text{ kPa}.$$

3.2 Data Acquisition

All data logging and recording operations are controlled by a mini-computer as shown schematically in Figure 4. Input signals are sampled by a scanning A/D converter (5 mV accuracy; 12 bit resolution; 55,000 readings per second). The amplitudes $s_{1,2,3}$ of the cw carriers can be sampled at rates up to 10 per second. To reduce the amount of data to be stored, daily records were produced at rates of 1 per second, including the meteorological readings of N_o, P, T (and rain rate R, mm/h). Data initially is stored in hourly segments on hard discs and periodically (about every two weeks) transferred to magnetic tape for archiving. Time series of eleven channels ($\underline{s_1}$, $\underline{s_2}$, $\underline{s_3}$, wide-band response, log (BER), $\underline{e}$, $\underline{RH}$, $\underline{N_o}$, $\underline{T}$, $\underline{P}$, R) for the current day are displayed on the computer terminal and copied once a day. Examples from the underlined channels have been selected for analysis.

3.3 Calibration Procedure (0.1-km Path)

An overall system stability for amplitude detection of better than ±0.5 dB was maintained for all of the three channels of the Boulder LOS experiment during the measurement period (August 1983 - June 1984). Calibrated mean signal levels permitted studies of water vapor attenuation at 28.8 and 96.1 GHz. Clear air amplitude scintillations have been recorded continuously with a sampling rate of 1 Hz. On a few occasions the rate was set to 10 Hz (maximum).

Table 4.
Performance Parameters for Boulder LOS Link
(Espeland et al., 1984)

Parameter	CHANNEL 1	CHANNEL 2	CHANNEL 3	Equation
	x = measured value			
f, GHz	11.4	28.8	96.1	
d, km	27.2	27.2	27.2	
L_o, dB	142.3	150.3	160.8 (0.105) (112.5)	28
P_t, mW	75	70	27.7 x	
dBm	18.75	18.45	14.42	
D_t, m	0.46	0.91	0.25	
G_t, dB	32.0 (4 deg)	46.0 (0.8 deg)	45.9 (0.85 deg)	26 (BW)
$\eta_{t,r}$	0.60	0.60	0.60	
D_r, m	0.46	0.91	0.30	
G_r, dB	32.0 (4 deg)	46.0 (0.8 deg)	47.9 (0.70 deg)	26 (BW)
L_t, dB	-2.0	-2.5	-0.62	
L_r, dB	-3.5	-1.0	-0.58	
L_M, dB	-8.5	-6.0	-5.5	
S_y, dBm	68.75	101.0	101.5	25
*) A, dB	0.33	2.18	10.3	Figure 6
			10.1 (0.371 dB/km)	Figure 13
†) P_r, dBm	-73.9	-51.5	-69.6	
	-74.5 x	-53.0 x	-69.5 x	
T_E, K	1900	1400	1210	
Δf, MHz	0.0015	0.0015	0.96	
Q_r, dBm	-134	-135	-108 x	29
F , dB	60 x	> 80 x	40 x	24

*) Measurement condition: v = 7.69 g/m³, T = 27°C, P = 83.4 kPa

†) $P_r = S_y - L_o - A$

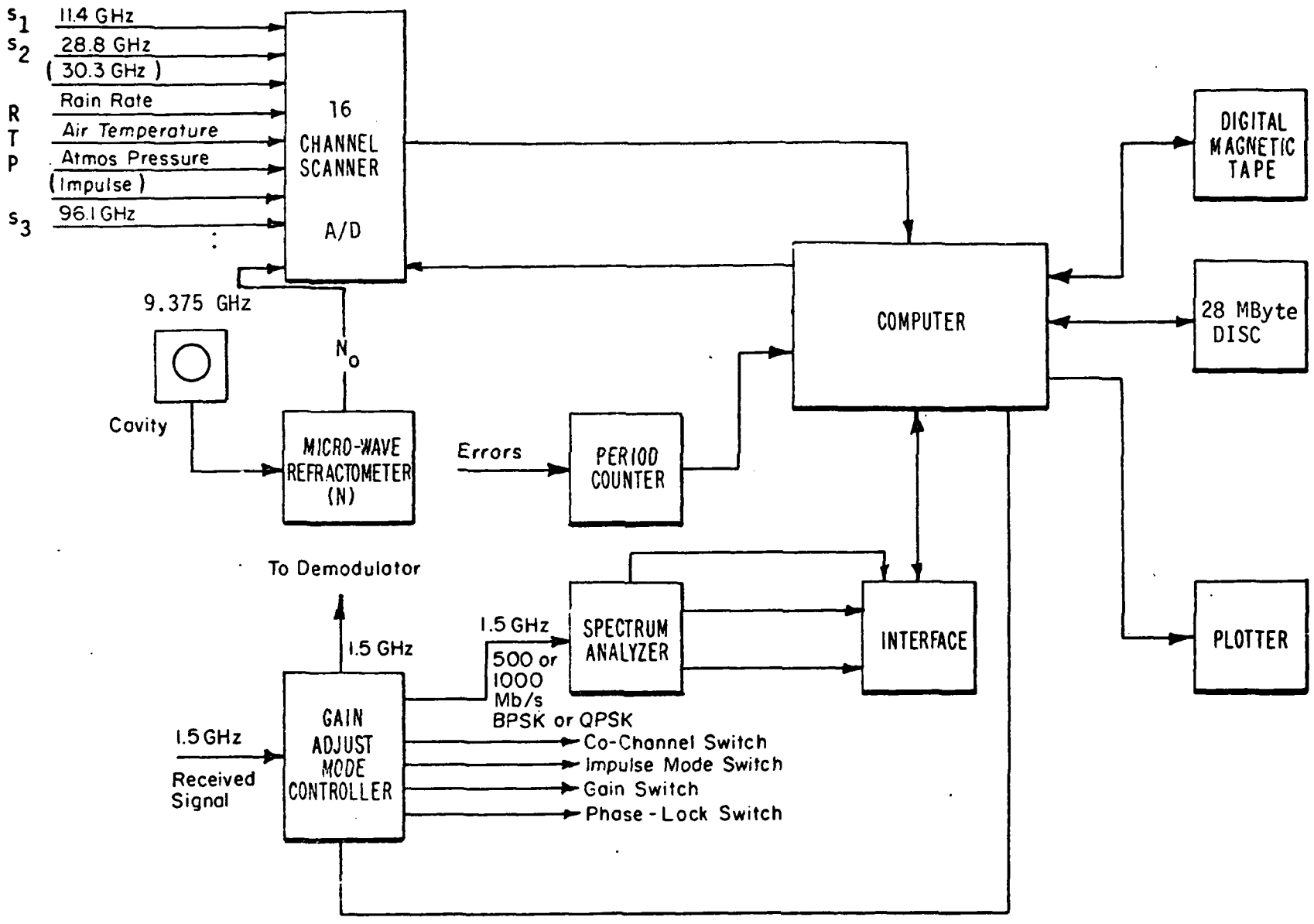

Figure 4. Schematic of data acquisition at RX (Espeland et al., 1984)

During the experiments the 96.1 GHz system was carefully calibrated four times. This was accomplished by shortening the propagation path length to $d(\gtrsim d_o) = 0.105$ km: free space loss L_o is reduced by 48.3 dB (from 160.8 to 112.5 dB) and atmospheric loss $A < 0.05$ dB $\cong 0$ is eliminated. The LOS system gain was compensated at the receiver by inserting an accurately (NBS) calibrated attenuator (58.3 ± 0.1 dB) to restore the originally received level to $s_3 = -10.0$ dB. In the short path configuration, experiments were performed to evaluate the 96.1 GHz receiver performance. The receiver noise power at the rf mixer was determined to be $P_r = -64.0$ dBm (see link budget in Table 4).

When the original path distance $d = 27.2$ km was restored, only atmospheric loss A and pointing error loss were left undetermined. Repetitive scans in elevation and azimuth at both the transmitting and receiving terminals assured main-beam alignment. Signal loss from pointing errors was reduced to less than -0.5 dB. This level of accuracy is accomplished by selecting optimum times for pointing (during periods of minimum scintillation) and by signal averaging. The overall uncertainty of the link calibration was estimated to be smaller than ±0.03 dB/km. For example, an experiment performed at 1315 MST on 9 August 1983 gave a differential path loss of 58.3 dB, by coincidence the same value as the attenuator used for the calibration path. The free space loss difference is 48.3 dB, hence the atmospheric loss $A = 10.0$ dB. The meteorological conditions at the receiver site were $P = 83.4$ kPa, $T = 27°C$ and $N_o = 260$ ppm. Equation (6) can be rearranged to read

$$v = (N_o - 2.588\ P\ \theta)/(5.768\ \theta - 0.028)\ \ g/m^3, \qquad (30)$$

which yields $v = 7.69$ g/m³ and leads to excellent agreement with the predicted value $A = 10.3$ dB (see Figure 6 and Table 4). Detection of path loss A at 28.8 GHz was possible by a relative calibration to $s_2 = 0$ dB from a "best" fit of the experimental data to predicted values (see Figure 13).

4. OBSERVATIONS, PREDICTIONS, AND RESULTS

In clear-air propagation of millimeter waves, weather-related changes of atmospheric refractivity (N) are mainly responsible for level changes and short-term fluctuations of received signal amplitudes (s_i). The propagation effects of attenuation, scintillation, and delay dispersion within the signal bandwidth reduce the fade margin (F) of a system. The program MPM, described in Section 2, is a valuable aid to support planning decisions for anticipated systems and to make performance assessments. On a more basic scale, measurements of α and β reveal information on molecular

interactions, and RSL scintillations offer insights into atmospheric dynamics.

Experiments have been conducted, including the one described in Section 3, producing data that are useful to verify various aspects of the highly structured millimeter-wave refractivity N (i.e., program MPM). In this section, results are presented regarding frequency-humidity-temperature dependences of attenuation and, for one case, of associated delay dispersion. From the Boulder LOS experiment, the daily records depicted in Figure 5 are presentations of minimum/maximum and strongest anomalous scintillation behaviors, selected from almost continuous records covering an 11 month period. The spectral density $W(\omega)$ of amplitude scintillations at 11.4, 28.8, and 96.1 GHz during these events is calculated.

4.1 Received Amplitude Levels

Time series $s_{1,2,3}(t)$ have been recorded and particular events are analyzed for the behavior of mean $\bar{s}$ and variance

$$\sigma_s = (n - 1)^{-1} \sum_n (\Delta s_n / \bar{s})^2 \quad dB^2,$$

with n the number of samples. Daily summary records containing selected event segments are depicted in Figure 5 for four cases: (a) a relatively quiet period ("dry" scintillations), (b) a relatively active period ("moist" scintillations), and (c) a stretch of rapid and severe up-and-down fades (possible multipath effects). In addition, 5d displays a rain event to demonstrate its severe influence--but precipitation will not be a topic in any discussion to follow. A statistical analysis usually reveals a log-normal cumulative probability distribution for periods (~ 10 min) of stationary conditions (e.g., Cole et al., 1978).

The power spectra of the amplitude scintillations were computed using the method of averaged modified periodograms (Oppenheim and Schafer, 1975). The Blackman window (Harris, 1978) was used and normalized for a coherent gain of unity (x 2.38). Modified periodograms were computed for segments of 256 points (sampled at a 1 Hz rate) to estimate the high frequency portion of the spectrum. The data for the time period of interest were then averaged in blocks of 256 points and segments of 16 points used to estimate the low frequency portion of the spectrum.

For purposes of clarity in the graphical presentation of the ratios of the spectra, the averaged periodograms were smoothed so that the points would be equally spaced in frequency on the logarithmic scale before the ratios were calculated. This was done by block averaging, beginning at the spectral point lowest in frequency and increasing the number of points averaged as the frequency increased.

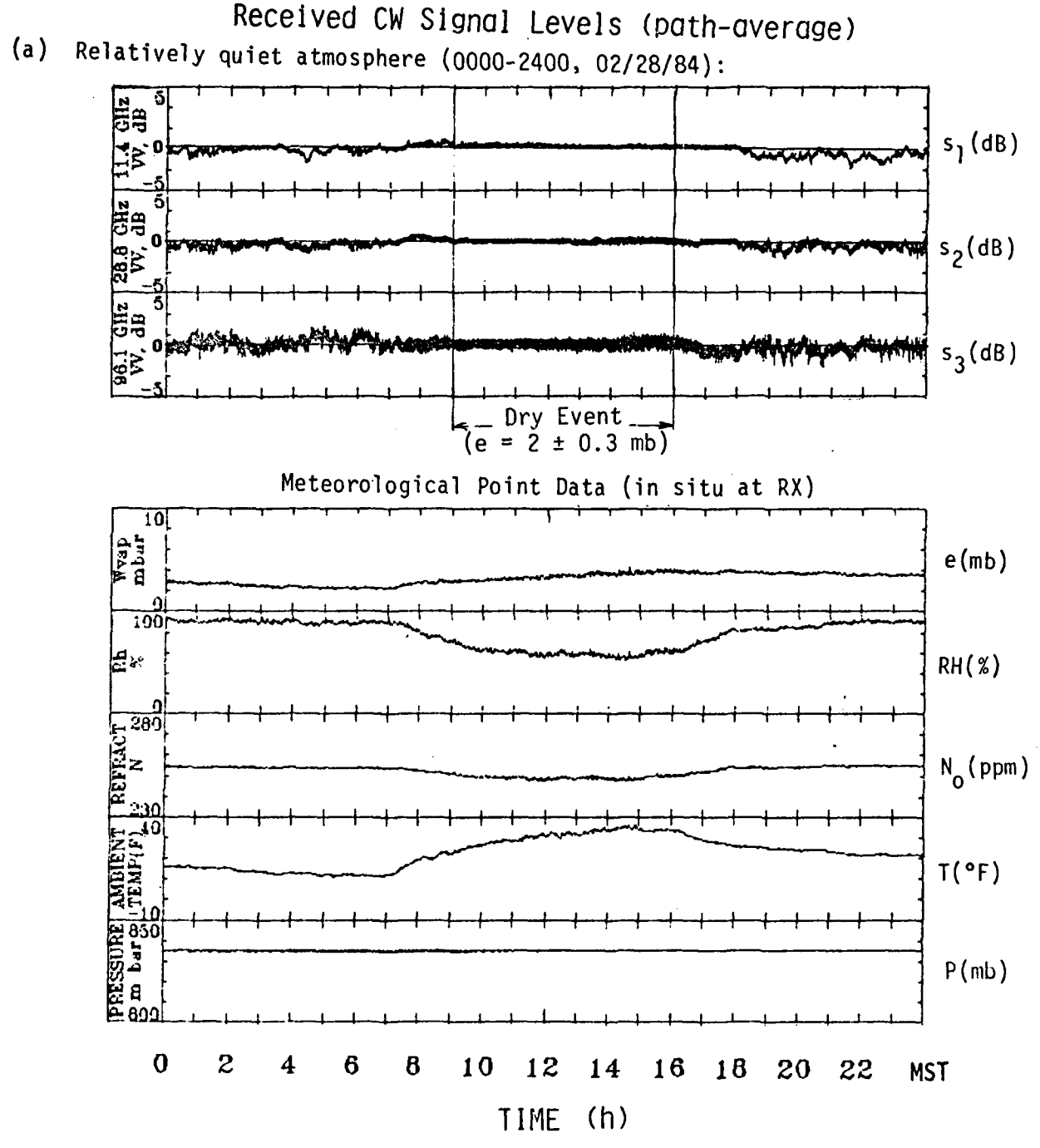

Figure 5 a-d. Typical daily records of received signal levels $s_{1,2,3}$ and supporting meteorological data for Boulder LOS link (L = 27.2 km) taken at a sampling rate, τ = 1s:
a) relatively quiet atmosphere ("dry" scintillations)
b) relatively active atmosphere("moist" scintillations)
c) possible multipath event
d) rain event

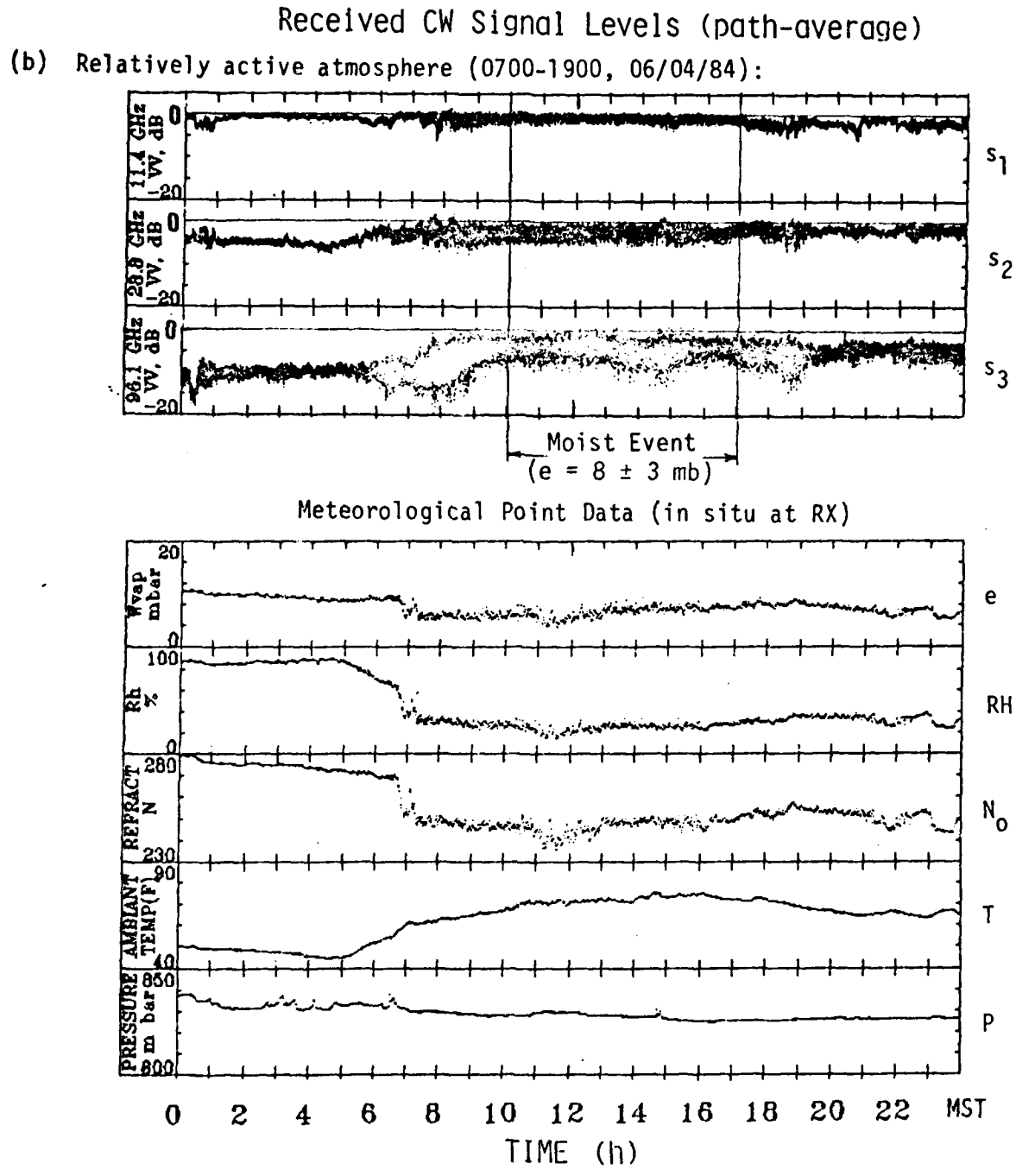

Figure 5. continued (b)

(c) Possible multipath event (0600-0900, 05/19/84):

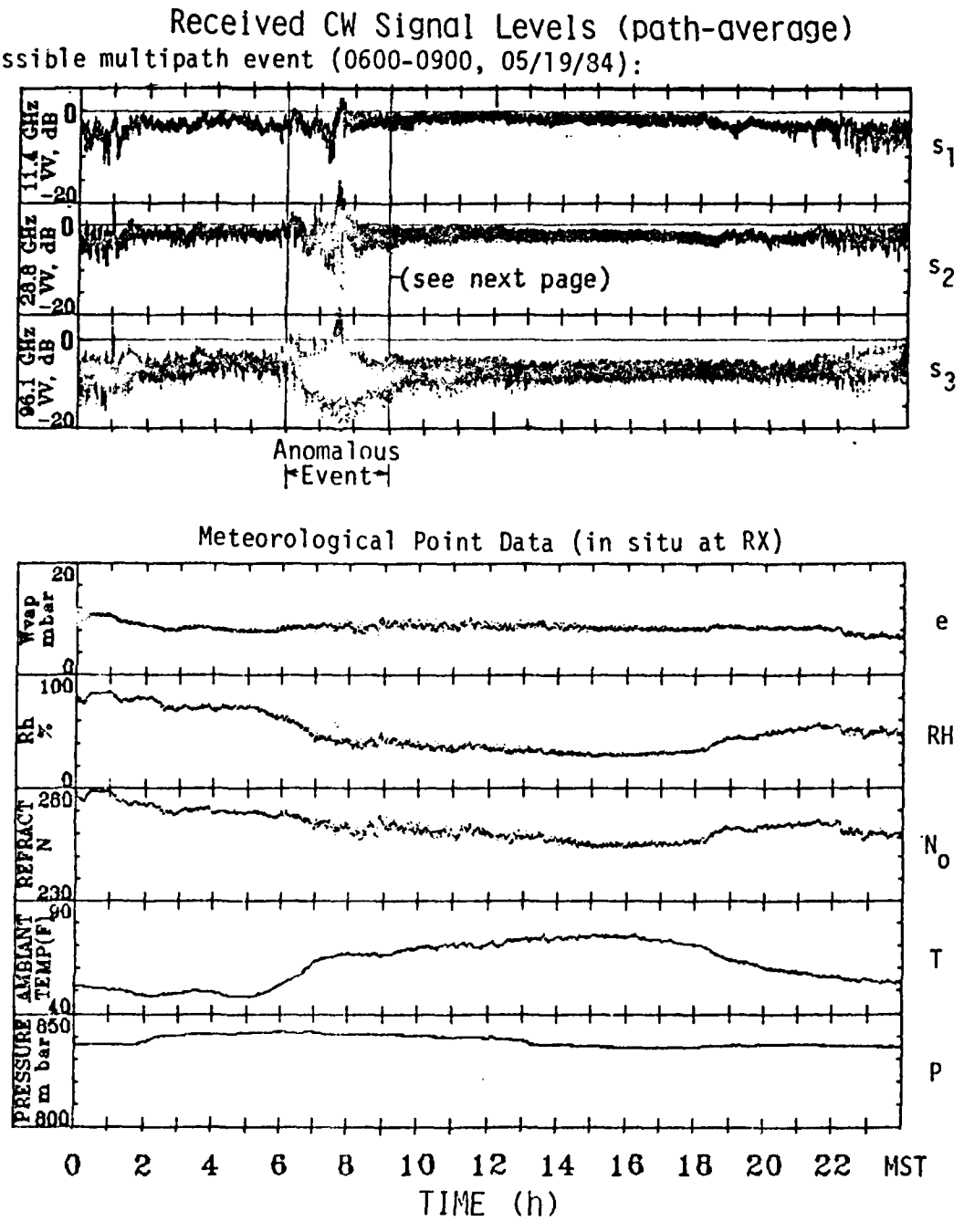

Figure 5. continued (c)

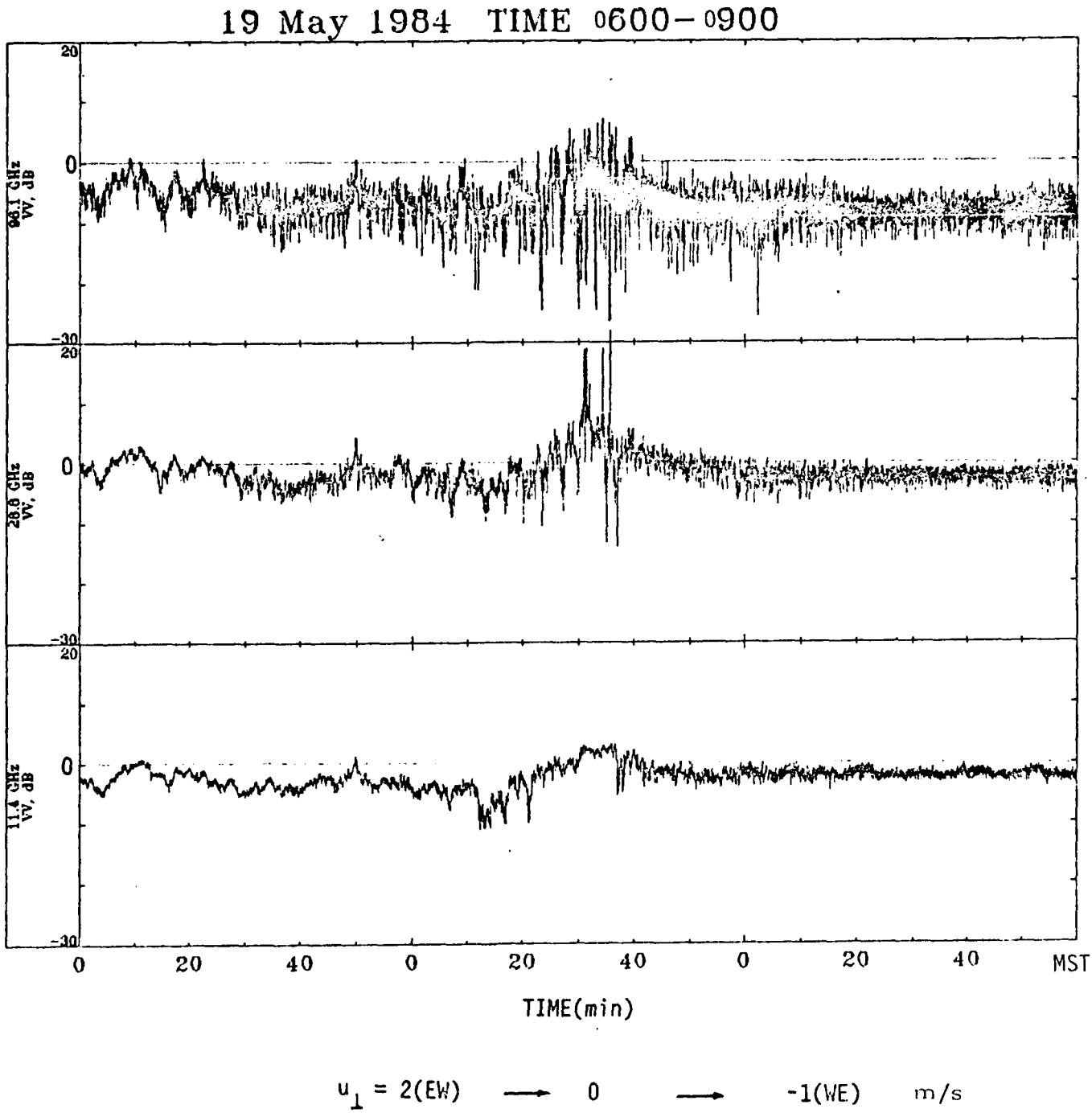

Figure 5. continued (c)

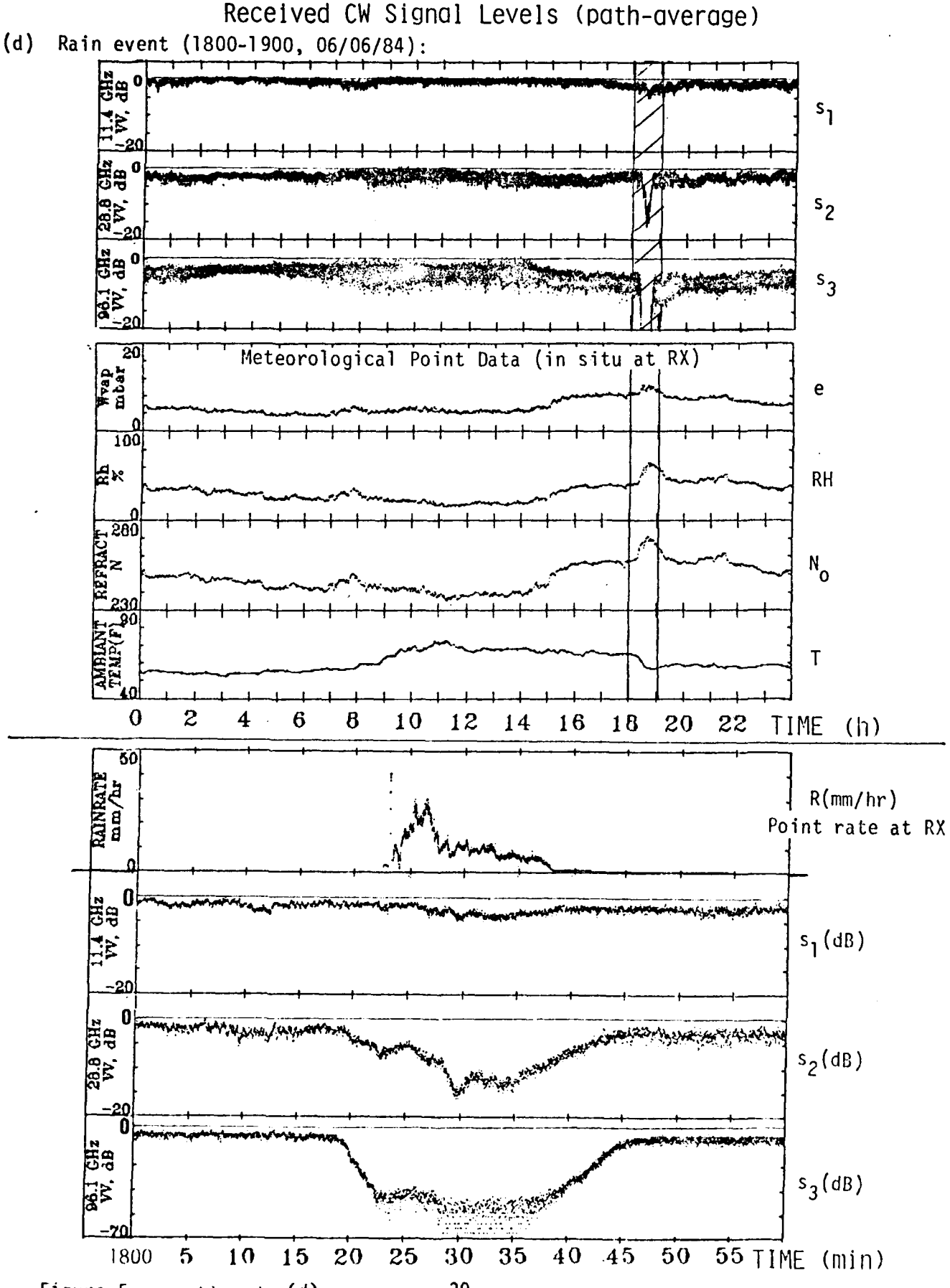

Figure 5. continued. (d)

Specifically, the number of points in each block was doubled beginning with a block of one point for the lowest frequency.

Amplitude scintillations are affected by temperature and humidity fluctuations along and wind across the radio path. To check how well the assumptions of turbulence theory [see above (16)] were met, data could be drawn from an extensive network of meteorological observation stations. In situ climatology within 5 km proximity of the test path was recorded by five different groups:

Acronym		Organization	# of stations available
LOS	Boulder test link, receiver site	NTIA-ITS.S	1 (see Fig. 5)
BAO	Boulder atmospheric observatory	NOAA-WPL	1 (10 m level)
BMW	Boulder wind observatory	NOAA-WPL	4
PROFS	surface mesonetwork	NOAA-ERL	3
MAYPOLE	surface mesonetwork	NCAR-MRS	6

and made available to ITS. Special thanks for exemplary cooperation is in order for Dr.'s Chandran Kaimal (BAO), Alfred Bedard (BMW), Peter Mandics (PROFS), and Ms. Cindy Mueller (MAYPOLE).

4.2 Predicted Responses

Clear air transmission effects formulated by (1)-(3) represent ultimate performance limitations to millimeter-wave applications. The MPM program was developed to be valid for frequencies up to 1000 GHz. Computer-efficient operation is assured by using only a limited local line data base (Table 2) of the major absorbers H_2O and O_2, supplemented by continuum spectra (12)-(14) including a suspended droplet (haze, fog) term. Humidity response of specific attenuation $\alpha(v)$ was predicted for the Boulder LOS link as displayed in Figure 6. Useful data to confirm predictions can be expected only at 96.1 GHz since the gain stability of the test link is on the order of ±0.05 dB/km.

The combined influence of both absolute (v) and relative (RH) humidity upon attenuation is made clear by analyzing the temperature dependence of a water vapor attenuation slope

$$g = [\alpha(v) - \alpha(v=0)]/v \qquad (dB/km)/(g/m^3).$$

Results of g(T) are presented in Figure 7 for three cases: (a) for frequencies of the Boulder LOS link, (b) for two water vapor line peaks, and (c) for centers of

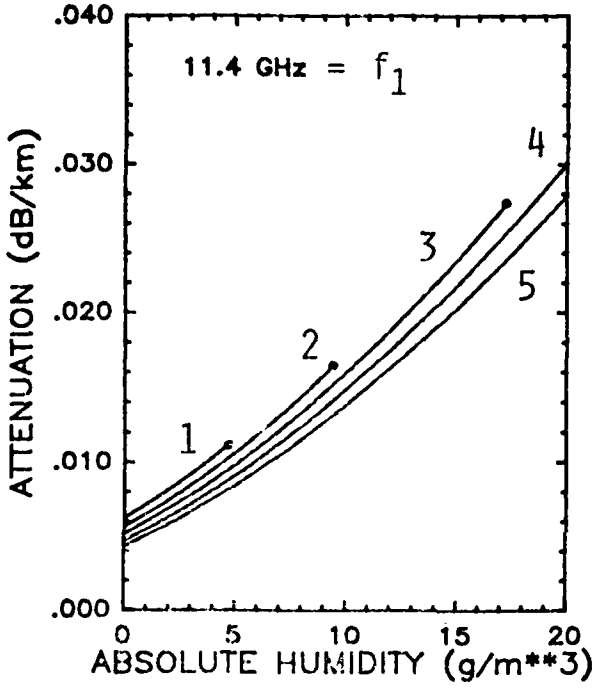

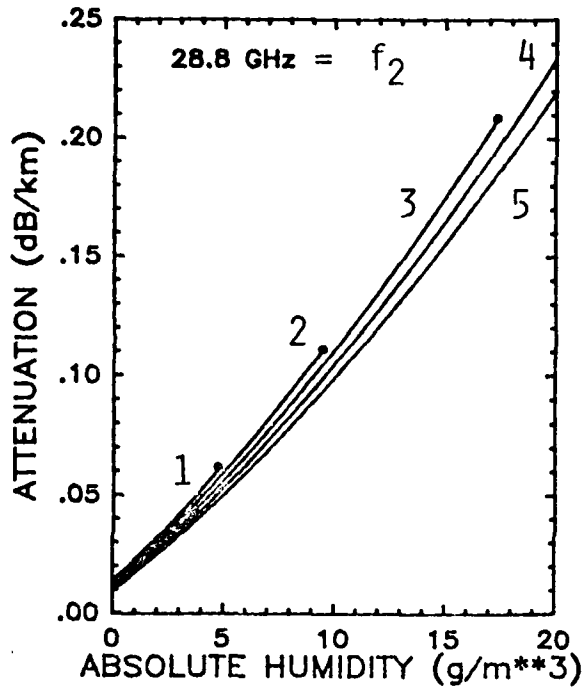

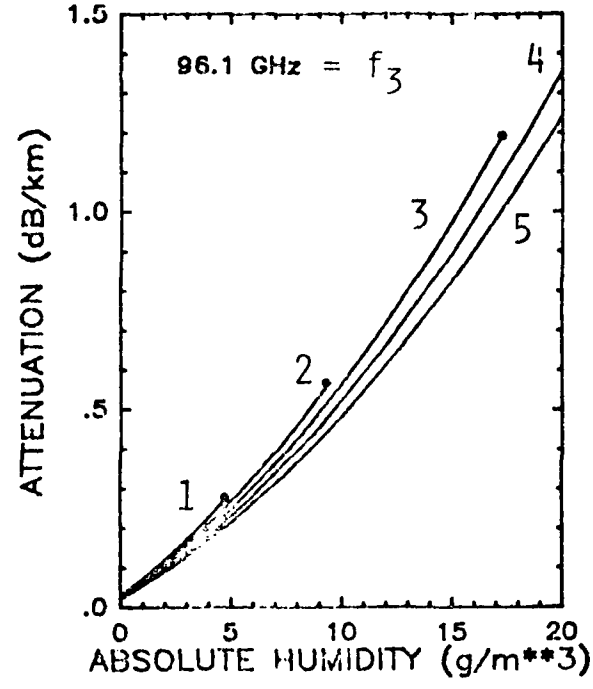

BOULDER LOS

d = 27.2 km
h = 1.65 km
P = 82.0 kPa

Curve ID	T (°C)
1	0
2	10
3	20
4	30
5	40

Figure 6. Predicted specific attenuation α for humid air and temperatures every 10°C ranging from 0° to 40°C at the three frequencies $f_{1,2,3}$ of the Boulder propagation path:
- RH = 100%

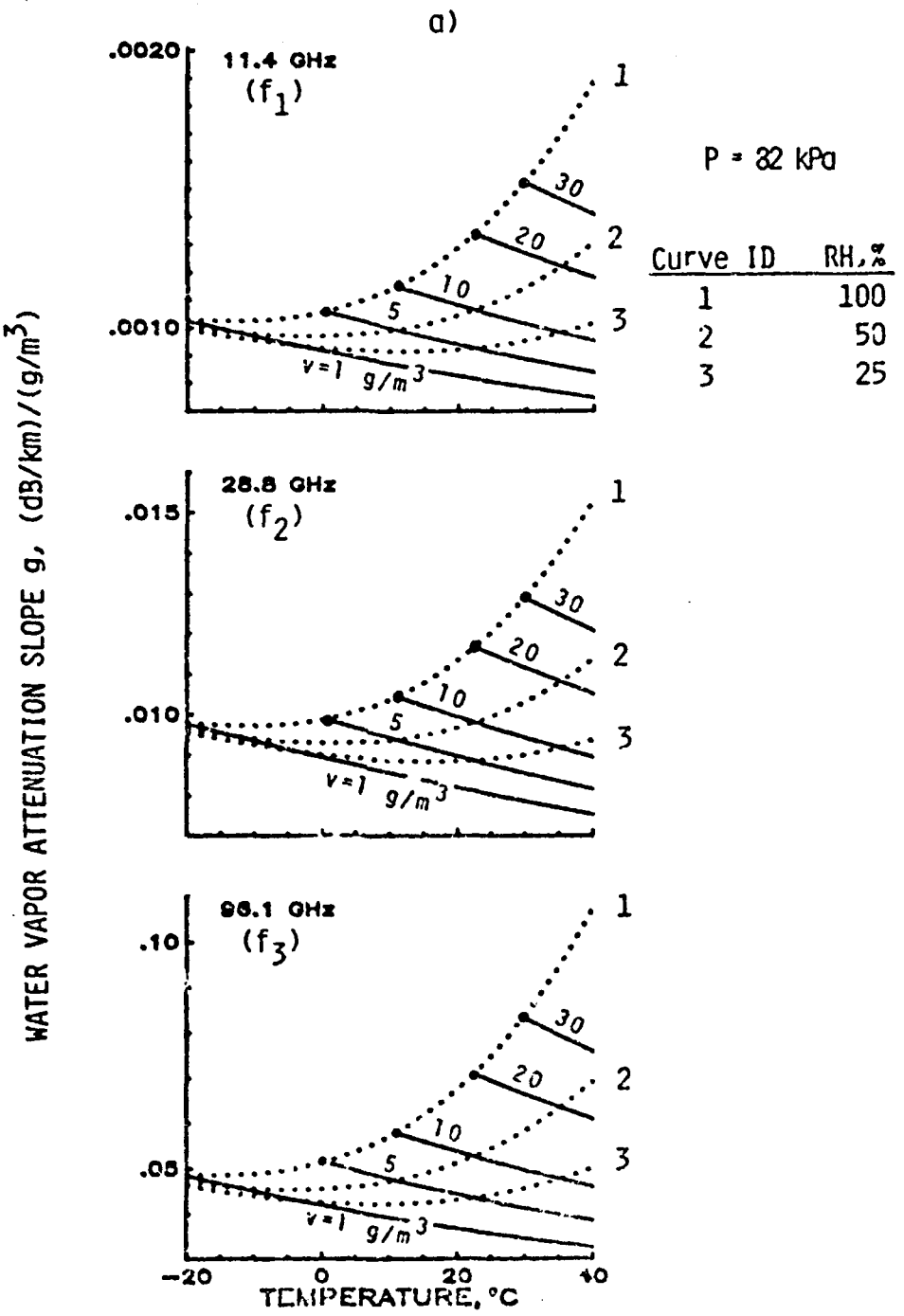

Figure 7. Water vapor attenuation slope $g = [\alpha(v) - \alpha(0)]/v$ as a function of temperature (solid curves are v=const., dashed curves are RH=const.) at different frequencies:

a) Boulder LOS link frequencies $f_{1,2,3}$ (see Figure 6)

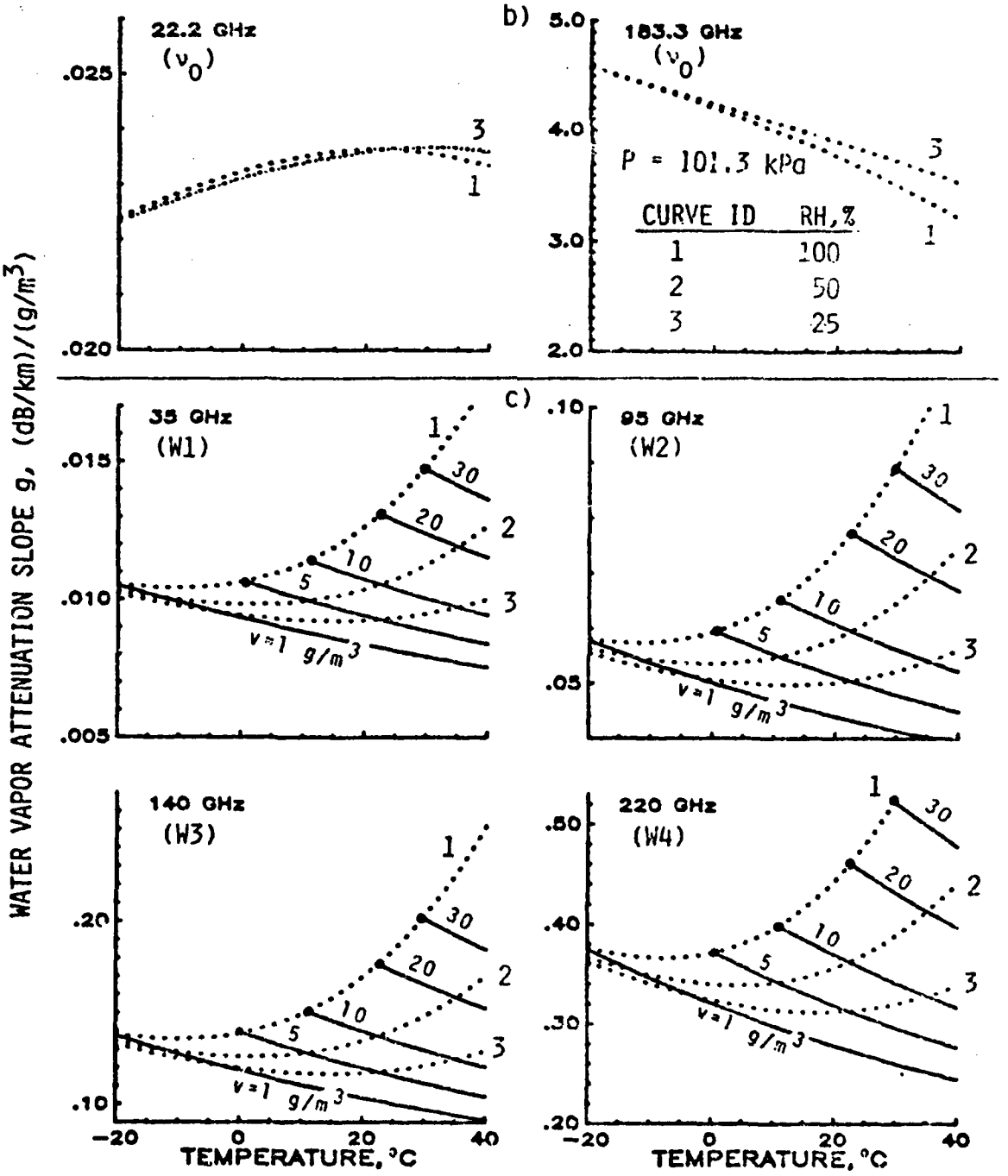

Figure 7. continued...

b) H_2O line center frequencies (2x)

c) atmospheric transmission window frequencies (4x)

four atmospheric windows W1 to W4 (see Figure 2). Corresponding numerical values of specific attenuation $\alpha(RH)$ in Table 5 span a wide range at sea level conditions. MPM predictions have to cover reliably values between 0.01 and > 140 dB/km.

Attenuation α_w due to suspended droplets (Figure 2, curve #9) is added to saturated air conditions that attenuate at rates $\alpha_s(100\%RH)$. The selected droplet concentration of $w = 0.1$ g/m^3 is representative of a fog with about 0.3 km optical visibility. A hydrosol factor

$$x_w = (\alpha_w/\alpha_s)(v_s/w)$$

is introduced in Table 5 to demonstrate, particularly in the window ranges, a strong increase in attenuation per unit of H_2O absorbers when vapor molecules convert into droplets. Typically, $w \leq 0.01$ for haze and $w > 0.1$ to 1 for fog conditions.

A strong, nonlinear influence of atmospheric humidity RH(T), v(RH), and w(RH) on millimeter-wave attenuation is predicted and elucidated by selected examples (see Figures 6, 7 and Table 5). To what extent experimental evidence is supported by MPM predictions will be investigated in the remainder of this report.

4.3 Model-Versus-Reported Data

Corroborative experimental data of sufficient quality to scrutinize predictions are scarce. Reliability, precision, and limited scope of supporting meteorological data often compromise the accuracy of results deduced from field observations. Generally, laboratory experiments provide more precise tests by simulating controlled electromagnetic and atmospheric conditions crucial to model validations. In this manner, contributions from the 22 and 183 GHz water vapor lines and 48 to 70, 119 GHz oxygen lines have been evaluated as summarized by Liebe (1981, 1983, 1985). Confirmation is lacking in window ranges W2 to W5 (see Figure 2) that are sensitive to the water vapor continuum (13). To test the MPM program, reported data sets on humidity-dependent propagation effects were chosen. The data have been gathered recently at different locations under various conditions. An overview of the experiments is given in Table 6. Reported data are generally available in graphic form and had to be digitized by us for a comparison with model predictions.

The first example, Figure 8, is unique--not only are attenuation rates $\alpha(v)$ reported at the frequencies $f_1 = 81.84$ and $f_2 = 245.52$ GHz, but also included are data on the associated differential dispersion (7b), (2b)

$$\Delta N(v) = \Delta\beta/3.336 = N'(f_2) - N'(f_1).$$

Table 5.

Predicted Specific Attenuation α (dB/km) for a Total Pressure P = 101.3 kPa and Hydrosol Attenuation Factor x_w at Various Relative Humidities RH (%) and Temperatures T(K) for Selected Millimeter-Wave Frequencies

Parameters			Hydrosol Factor	Specific Attenuation α of Air				
f	T	v_s	x_w	100% RH	75% RH	50% RH	25% RH	0% RH
GHz	K	g/m^3		dB/km				
22.2	310	43.46	8.4	1.03	0.78	0.52	0.27	0.011
	300	25.49	10	0.62	0.46	0.31	0.16	0.012
(v_o)	290	14.31	13	0.35	0.27	0.18	0.10	0.013
	280	7.65	17	0.19	0.15	0.10	0.06	0.014
	270	3.87	22	0.11	0.08	0.06	0.04	0.016
	260	1.85	29	0.06	0.05	0.04	0.03	0.017
35.0	310		26	0.76	0.50	0.29	0.13	0.026
	300		41	0.38	0.27	0.17	0.09	0.028
(W1)	290	"	60	0.20	0.15	0.10	0.06	0.031
	280		84	0.12	0.09	0.07	0.05	0.034
	270		114	0.08	0.07	0.06	0.05	0.038
	260		135	0.06	0.06	0.05	0.05	0.042
95.0	310		28	4.56	2.89	1.58	0.63	0.036
	300		44	2.18	1.44	0.83	0.37	0.040
(W2)	290	"	62	1.05	0.73	0.45	0.22	0.044
	280		79	0.53	0.38	0.26	0.14	0.048
	270		90	0.28	0.21	0.16	0.10	0.053
	260		89	0.16	0.14	0.11	0.08	0.058
140.0	310		24	10.21	6.48	3.54	1.39	0.019
	300		35	4.88	3.21	1.84	0.78	0.021
(W3)	290	"	46	2.34	1.60	0.97	0.44	0.023
	280		53	1.13	0.80	0.51	0.25	0.025
	270		54	0.56	0.41	0.27	0.15	0.027
	260		48	0.28	0.21	0.15	0.09	0.029
183.3	310		3.0	143.08	109.98	75.43	38.96	0.014
	300		2.9	91.32	69.60	47.22	24.07	0.016
(v_o)	290	"	2.7	54.94	41.59	28.01	14.16	0.017
	280		2.5	31.10	23.44	15.71	7.91	0.018
	270		2.1	16.54	12.44	8.32	4.18	0.019
	260		1.7	8.24	6.19	4.14	2.08	0.020
220.0	310		18	26.23	16.73	9.19	3.62	0.016
	300		23	12.64	8.35	4.81	2.04	0.018
(W4)	290	"	27	6.10	4.18	2.52	1.14	0.019
	280		28	2.97	2.10	1.32	0.63	0.021
	270		25	1.45	1.06	0.69	0.34	0.022
	260		20	0.70	0.53	0.35	0.19	0.023
Curve ID (Fig. 2, Fig. 7b,c)			-	8 1	7 -	6 2	5 3	1 -

Table 6.

Overview of Experimental Results From Horizontal Line-of-Sight (LOS) Paths, a Mountain Peak Zenith (ZEN) Path, and Laboratory (LAB) Experiments, All Used As Corroborative Data for the Propagation Program MPM

Test Frequency f	Figure	Path Type	Path Length d	Expon. y	Reference
GHz			km	(T^{-1} law)	
81.84	8	LOS	0.81		a
245.52	8	LOS	0.81		a
337	9	LOS	0.50	6(2)	b
94	10	LOS	0.94		c
192-260	11	LOS	1.5	3.6(1.3)	d
335-418	12a	LOS	1.58		e
330-430	12b	LAB	1.58		e
138.2	(Eq. 13a)	LAB	(equiv. 0.15)	4.0(1.5)	f
96.1	13, 6	LOS	27.2	5(2)	-
2.5-10.0	(Table 7)	ZEN	(h_o = 3.80)		g

a = Manabe et al., 1984

b = Gasiewski, 1983

c = Buijs and Janssen, 1981

d = Fedoseev and Koukin, 1984

e = Furashov et al., 1984

f = Liebe, 1984

g = L. Danese, personal communication, 1984

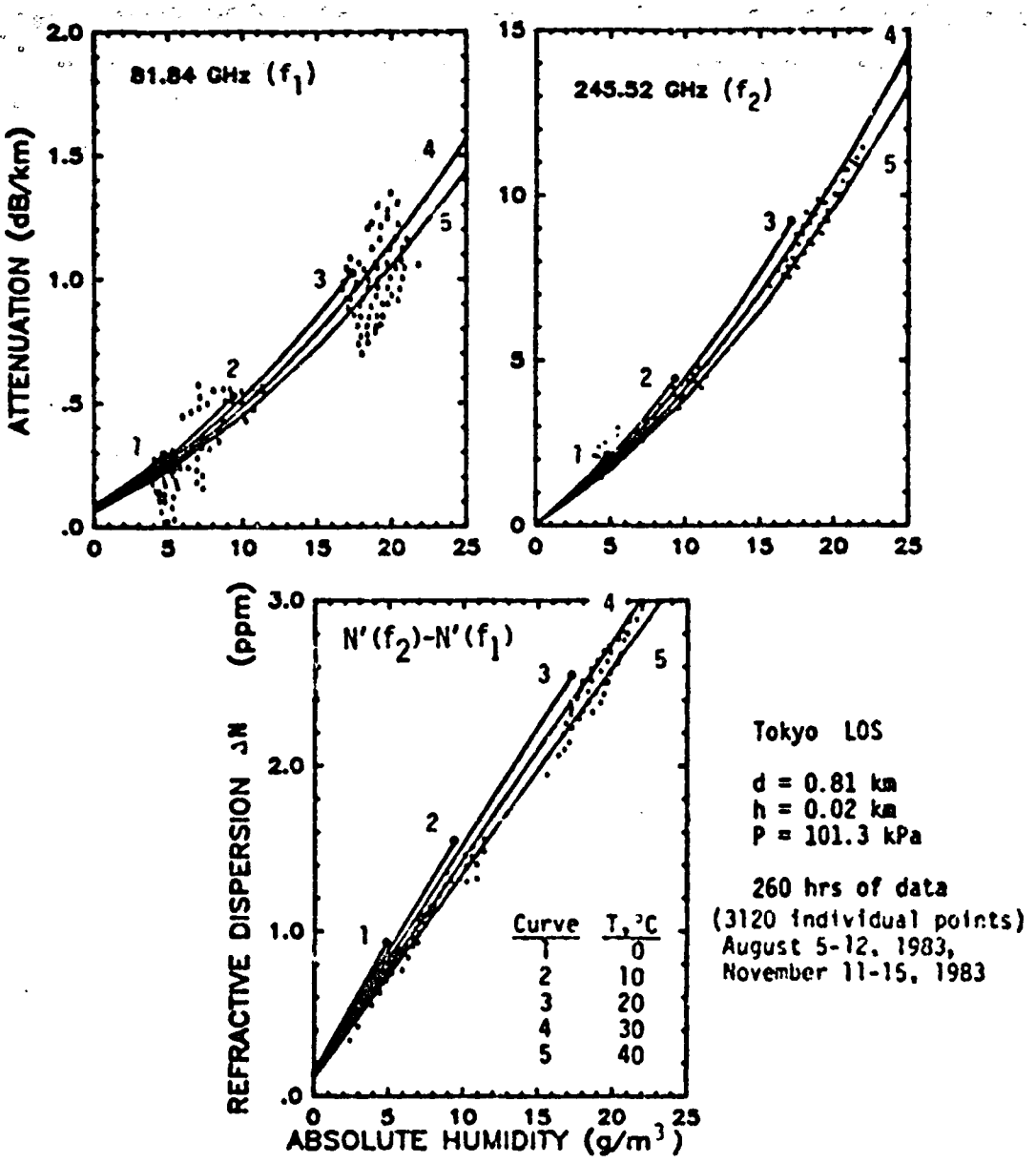

Figure 8. Specific attenuation α and refractive dispersion $\Delta N = N'(f_2) - N'(f_1)$ for humid air and temperatures every 10°C ranging from 0° to 40°C at two frequencies $f_{1,2}$ of a Tokyo propagation path:
• Representative of measured data clusters (Manabe et al., 1984)
— MPM, • RH = 100%

The curves in Figure 8 were produced by simulating reported meteorological conditions and then superimposing the experimental data. Clusters of original points were condensed into dots in the course of the digitizing process. The gain stability of this LOS experiment was estimated to be better than ±0.3 dB/km over a temperature range of 0° to 40°C. Good agreement is displayed between model and experimental data on both attenuation and dispersion. When contrasted with the attenuation rates $\alpha(\nu)$, an almost linear dependence with absolute humidity v can be observed for dispersion $\Delta N(\nu)$. Theoretically, outside a line center frequency range $\nu_o \pm 5\gamma$, refractive dispersion $N'(f)$ is independent of a particular shape function $F'(f)$ which makes the correction (13b) for H_2O line contributions above 1 THz quite reliable. Equation (13b) was formulated by fitting line-by-line calculations [$N'(H_2O$ spectrum) - N'(lines < 1 THz)] that were made available by R. Hill (personal communication, 1984). The next example, Figure 9, pertains to an LOS experiment performed at 337 GHz in Sandusky, Ohio, at temperatures from 12° to 25°C. Figure 9 shows one data set $\alpha(\nu)$, out of 18, selected over a narrow temperature range 16° ± 1°C.

A different type of effect is often neglected in millimeter wave propagation, namely that depending on relative humidity. Atmospheric air always contains a certain mass concentration w of hygroscopic aerosol; for example, some typical values are

$$w_o\ (RH \leq 10\%) = 10^{-6}\ \text{(clean air) to } 5 \times 10^{-4}\ \text{(polluted air) g/m}^3,$$
$$w\ \ (RH \geq 50\%) = 10^{-4}\ \text{to } 1 \times 10^{-2}\ \text{g/m}^3.$$

Water vapor-to-droplet conversion follows roughly (5) up to 96% RH. Growth functions valid for the range RH > 96 to 101% are not easily available (e.g., see Haenel, 1976). Data of $\alpha(\nu,RH)$, acquired close to the seashore in The Netherlands at both 94 GHz and optical frequencies (visible light) are displayed in Figure 10. All values exceeding $\alpha(\nu)$-predictions are bunched close to RH = 100% where haze transforms into fog. Hence, attenuation excesses are explained via (14a) by hydrosol concentrations up to $w \geq 0.2$ g/m³. Optical attenuation (Mie scattering theory) places the boundary (visibility) between haze and fog at about 5 dB/km.

Water vapor attenuation data for frequencies between 195 and 340 GHz are compared with model predictions in Figures 11 and 12. Results for the range f = 330 to 430 GHz include field (8.5°C, 8.4 g/m³, 99%RH) and laboratory (25.5°C, 19 g/m³, 80%RH) data taken in the U.S.S.R. (Figure 12). Considering the multifarious difficulties that plague absolute calibrations, the comparisons of model-vs.-experimental data are encouraging. No anomalous absorption features have been uncovered.

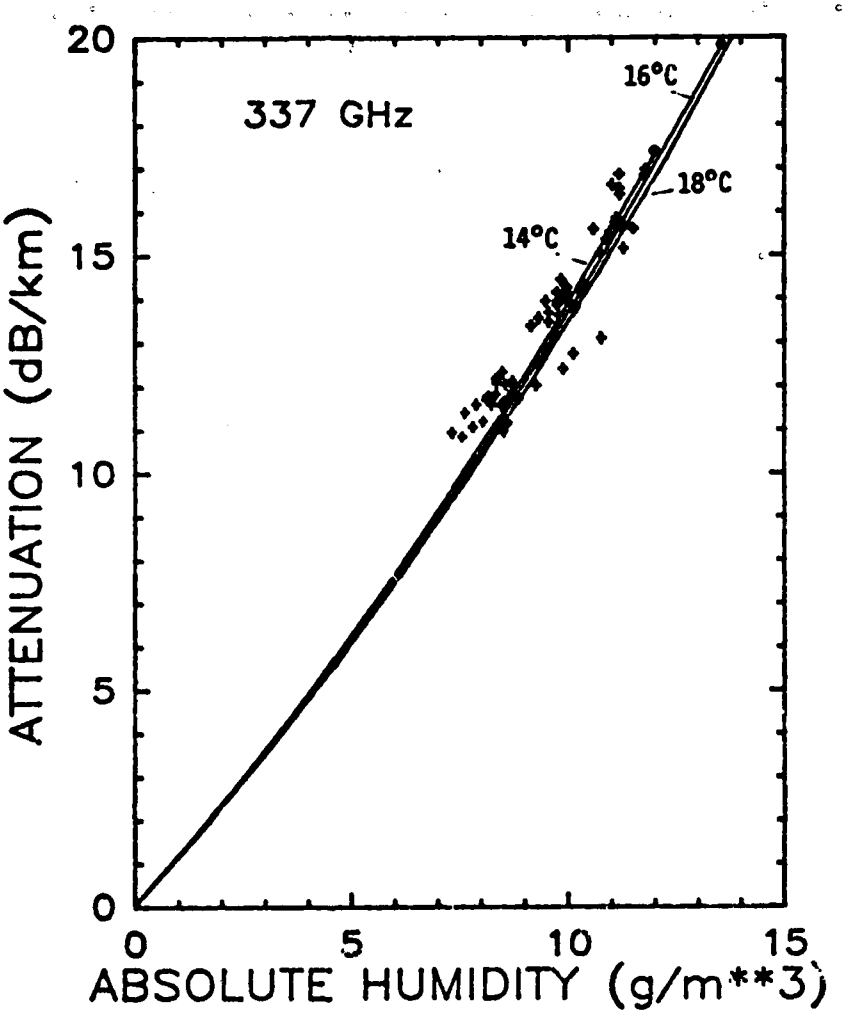

Sandusky LOS

d = 0.50 km
h = 0 km
P = 101.3 kPa

Figure 9. Specific attenuation α for humid air at T = 16 ± 2°C and a frequency of 337 GHz:
+ Measured data (Gasiewski, 1984)
— MPM, • RH = 100%

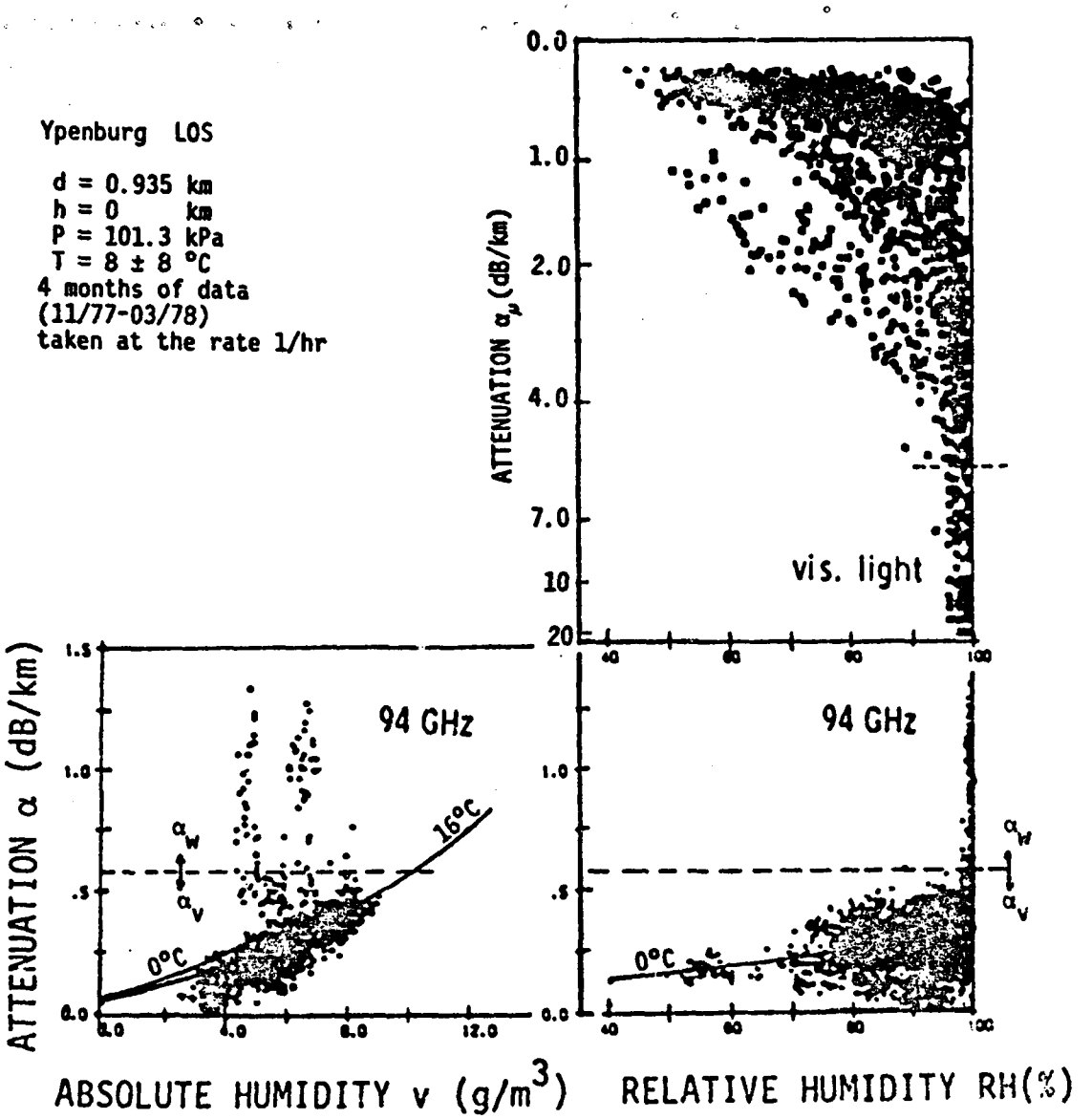

Figure 10. Attenuation rates α at 94 GHz and optical frequencies (visible light) as functions of absolute humidity v and relative humidity RH:
•, • Measured data (Buijs and Janssen, 1981)
——— MPM

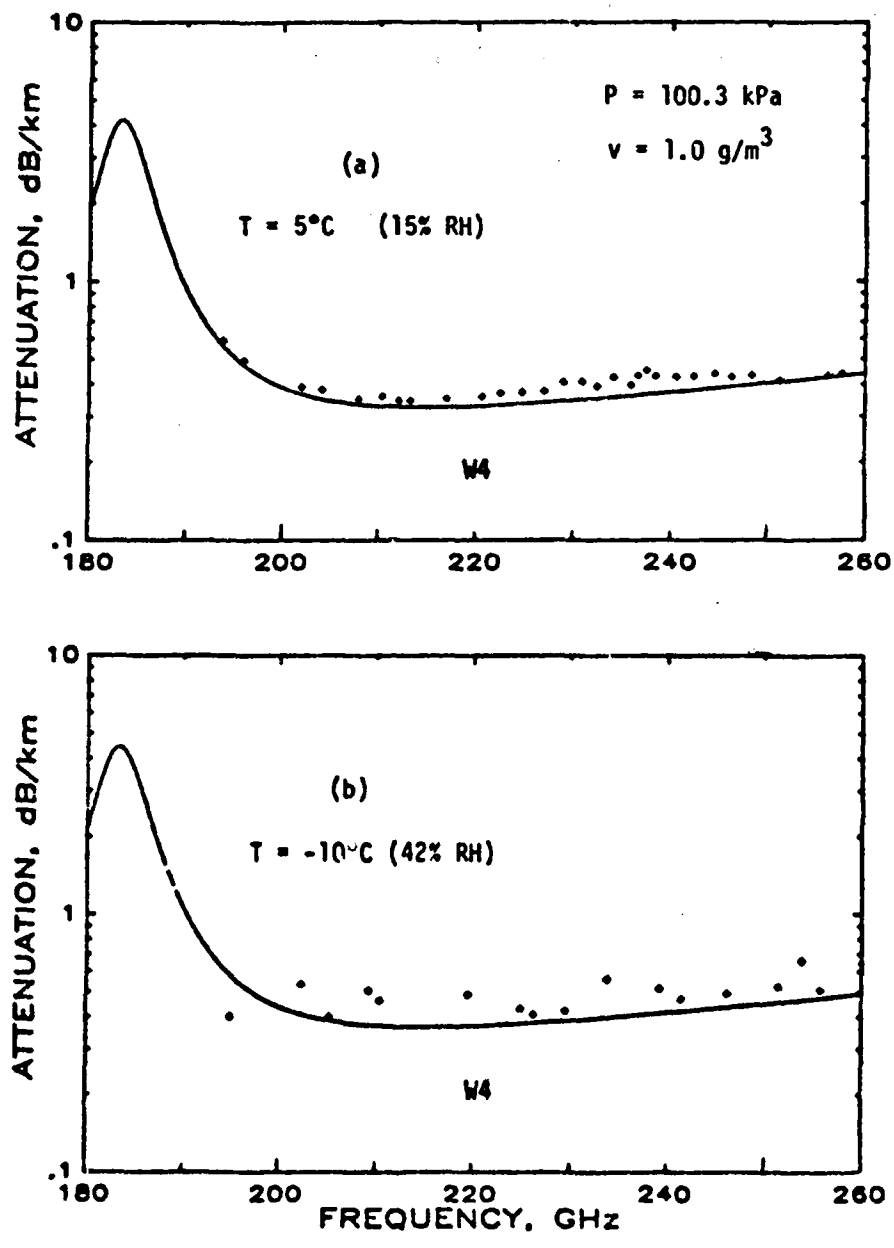

Figure 11. Water vapor attenuation rates $\alpha(v)$ across the atmospheric window range W4 at two temperatures, 5° and -10°C:
+ Measured data (Fedoseev and Koukin, 1984)
—— MPM

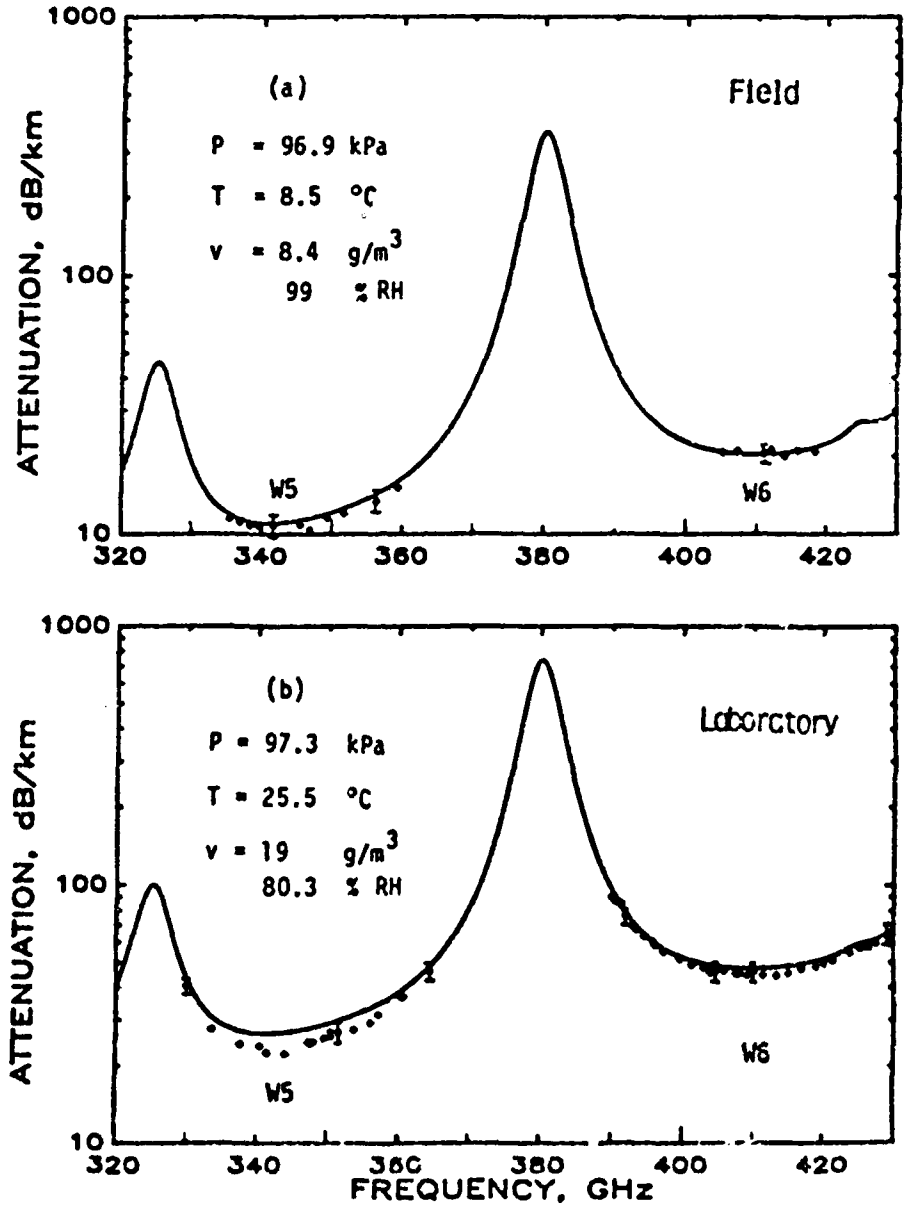

Figure 12. Water vapor attenuation rates $\alpha(v)$ across the atmospheric window ranges W5 and W6 at two temperatures, 8.5°and 25.5°C:
+ Measured data (Furashov et al., 1984)
—— MPM

Analysis of raw data $\alpha(v,T)$ available from the experiments allows an estimate of the negative temperature dependence θ^y. The exponent y was found to vary between 3.5 and 6 (Table 5), which is consistent with semiempirical theoretical results (Liebe, 1985).

Path attenuation $A = A_p + A_v$ and atmospheric noise expressed by a brightness temperature $T_B = T_p + T_v$ are closely related (e.g., Waters, 1976). Brightness temperatures T_B^x have been measured at six frequencies between 2.5 and 90 GHz in clear weather with radiometers looking toward zenith from a mountain peak. At h_o = 3.80 km, a typical tropospheric water vapor content V (mm) is reduced to about one-fifth. In fact, an average water vapor content was determined to be

$$V = \int_{3.8\ km}^{\infty} v(h)dh \cong 3 \pm 1\ mm.$$

All experiments were conducted with utmost care for the purpose of measuring cosmic background radiation (2.8 K).

The MPM program was operated with a mean July climate for California that specified P(h), T(h), and v(h) profiles over the range h = 3.8 to 30 km. Dry air zenith attenuation A_p and a water vapor attenuation slope $a_v \cong A_v/V$ were calculated by numerical integration and listed in Table 7. Values of A_p have been converted into brightness temperatures T_p by assuming an average temperature T_o = 260 K consistent with the T(h) profile. Brightness data below 10 GHz are particularly sensitive to the correct value of γ_o in the dry air continuum (12a). Above 10 GHz, the water vapor slope a_v amounts to meaningful values. At 90 GHz, the data point $(T_x - T_p)/33$ = 1.70 K/mm was used as a reference water vapor slope z_v to define an "equivalent" temperature of 305 K for conversions from path attenuation to medium brightness at other frequencies. This way, all six T_B^x-data in Table 7 are apportioned in a consistent manner to dry and wet attenuation terms based upon MPM predictions.

In summary, good agreement between predicted and reported responses, foremost specific attenuation, was found over a wide range of parameters--test frequencies varied between 2.5 and 430 GHz and meteorological conditions as follows: P = 70 to 101 kPa, T = -10° to 35°C, v = 0 to 25 g/m³ and RH = 0 to 99%. All in all, some credibility can be given to the computer program MPM detailed in Section 2.1.

END

FILMED

2-86

DTIC